1.C

Nuclear Physics **A158** (1970) 1—42; © *North-Holland Publishing Co., Amsterdam*

NUCLEAR SATURATION AND THE SMOOTHNESS OF NUCLEON-NUCLEON POTENTIALS

MICHAEL I. HAFTEL †

Naval Research Laboratory, Washington D.C., 20390 ††

and

FRANK TABAKIN

University of Pittsburgh, Pittsburgh, Pa. 15213 ††

Received 6 July 1970

Abstract: The two-nucleon and nuclear matter problems are solved by matrix inversion in momentum space. Direct matrix inversion of the Lippman-Schwinger and Brueckner equations is shown to be useful for general nuclear potentials including ones that are local, nonlocal, weak, strong, central, or noncentral. This flexibility is employed to study the relationship between nuclear saturation and the smoothness of the two-nucleon interaction.

Five potentials are considered that give approximately equivalent phase shifts but differ in their smoothness. Two examples of smooth potentials with very weak nonlocal tensor terms are given. The potentials are classified according to their smoothness by calculating the wave function defect and the wound integral for each case.

The binding energy of nuclear matter is calculated for each potential using the effective mass and angle-averaged Pauli operator approximations. A self-consistent hole spectrum and a free particle spectrum are used.

A systematic dependence of saturation on the smoothness of the two-nucleon interaction is found. Only strong potentials with strong tensor terms yield correct saturation, whereas very smooth potentials produce overbinding and large equilibrium densities.

1. Introduction

The interaction between two nucleons is not determined uniquely by elastic scattering experiments. It is possible to fit two-nucleon data using very different potential forms. Some of these potentials are local with quadratic spin-orbit terms, others are local in each eigenchannel, others have short-range nonlocalities [1-3]). The essential difference between these potentials is not in their asymptotic wave functions, scattering amplitudes, or phase shifts, but rather in their wave functions at short distances. Information about the wave function can be obtained from inelastic processes [3]). However, it is difficult to extract this information and the short-range part of the wave function remains uncertain. If the detailed form of the two-nucleon wave function is not fixed by experiment, one should question the reliability of a many-body theory that begins with an uncertain interaction. Therefore, the role of the short-range part of the nucleon-nucleon interaction must be clarified.

† N.R.C.–N.R.L. Postdoctoral Resident Research Associate.

†† Supported in part by the US National Science Foundation.

In this paper, we study the dependence of nuclear binding energies on the form of the two-nucleon potential. Our procedure consists of considering several possible potential forms that yield fits to the nucleon-nucleon elastic scattering phase shifts. These various potentials are then classified according to their strength or smoothness. The binding energy of nuclear matter is calculated using these potentials of varying smoothness. It is concluded that strong potentials having strong tensor forces are needed to produce the correct saturation of nuclear energy and density.

To make this conclusion, we have dealt with a large class of potential strengths and forms. This large class of interactions, including ones that are extremely weak, are generated by introducing short-range nonlocalities. The nonlocalities are restricted to short distances, but are included in both central and tensor terms. In this way, potentials with extremely weak tensor forces can be constructed and examined.

The scattering and bound state solutions of the Schrödinger equation can be found numerically even for potentials with seemingly complicated nonlocalities. In sect. 2, a simple numerical matrix inversion method for solving the coupled channels Schrödinger equation in momentum space is presented. It is shown that the direct matrix inversion in momentum space is a precise and speedy method of solution that we prefer over the alternate possibilities of employing either the Weinberg or Noyes-Kowalski methods [4]). In fact, we find that direct matrix inversion can be applied to any finite potential, including ones that are local, nonlocal, central, noncentral, weak or strong.

This considerable latitude in choice of potential provides us with an important means of studying the mechanism of nuclear saturation. First a reliable means of solving the Brueckner equation for infinite nuclear matter is needed. Numerical matrix inversion in momentum spaces again proves to be a precise, rapid and convenient means of handling general nonlocal potentials. The procedures for solving the Brueckner equation are the same as for the free two-nucleon scattering case, but a few additional assumptions are employed. These assumptions are that one can use the angle averaged Pauli operator, that the effective mass approximation is valid for nucleons below the Fermi sea, and that there is zero single-particle potential for nucleons above the Fermi sea (sect. 3).

Having calculated the Brueckner G-matrix, the saturation curves (i.e. the binding energy per particle versus density) can be obtained for a variety of potentials. The potentials used here include the Yukawa-core Reid [1]) potential and the one-boson exchange potential (OBEP) of Bryan and Scott [5]).

Two new potentials are also presented (sect. 4). These phenomenological potentials have both local and nonlocal tensor forces and are adjusted to the triplet-even eigenphases for $L \leqq 2$. They differ from previous potentials in having extremely weak tensor terms, as is demonstrated in sect. 5. They are used here to clarify the role of tensor forces in nuclear saturation. Another example of a potential with nonstatic tensor forces, the Appel potential [6]), is also considered in sect. 5.

The binding energies and densities obtained using these potentials are presented in

sect. 5; the full self-consistency problem and higher partial waves are considered. The wound integral κ is calculated for each of the potentials and used as a measure of the potential's smoothness. The additional significance of κ is that it is the expansion parameter for nuclear many-body theory. The Bessel transforms of the wave function defect are also examined [7]) (sect. 5).

The calculation of κ and of the satuation curves reveals a definite relationship between saturation and smoothness. It is found that potentials with larger κ, i.e. stronger potentials, are needed to get the correct saturation. The most important contribution to κ comes from the tensor force and it is concluded that strong tensor forces are required by saturation (sect. 6).

A discussion of the restrictions placed upon potentials by these studies is given in sect. 6.

2. The two-body problem in momentum space

2.1. MOMENTUM SPACE

A simple matrix inversion method for solving the Schrödinger equation in momentum space is presented in this section. It can be applied to any nonsingular potential either local or nonlocal, central or noncentral. The use of matrix inversion in momentum space is by no means a new idea [8]). Several alternate approaches to solving the Schrödinger equation for general nonlocal potentials are also available in the literature [4, 9]). For the purely nuclear part of the two-nucleon interaction, we find that direct matrix inversion is simplest.

The Schrödinger equation describing the two-body relative motion is given by

$$\frac{\hbar^2}{M}\nabla^2\psi_n(\boldsymbol{r}) + \int \mathrm{d}\boldsymbol{r}\, V(\boldsymbol{r}|\boldsymbol{r}')\psi_n(\boldsymbol{r}) = E_n\psi_n(\boldsymbol{r}), \tag{2.1}$$

where M is the nucleon mass, $\boldsymbol{r} = \boldsymbol{r}_1 - \boldsymbol{r}_2$ denotes the relative displacement of the two nucleons, and E_n is the total relative energy. In general $V(\boldsymbol{r}|\boldsymbol{r}')$ is a nonlocal operator. For local potentials, $V(\boldsymbol{r}|\boldsymbol{r}') \to \delta(\boldsymbol{r}-\boldsymbol{r}')V(r)$, many rapid methods exist for solving the resulting second order differential equation. However, for nonlocal potentials one faces the difficult task of solving an integro-differential equation in configuration space. Numerical methods for that problem are also available and are particularly useful when Coulomb forces are to be included [9]).

An alternate approach, to be used here for nonlocal nuclear potentials, is to introduce momentum space. The relative motion is then described by

$$(k^2 - k_0^2)\psi_n(\boldsymbol{k}) = \frac{M}{\hbar^2}\int \mathrm{d}\boldsymbol{k}' V(\boldsymbol{k}|\boldsymbol{k}')\psi_n(\boldsymbol{k}'), \tag{2.2}$$

where $2\boldsymbol{p} = \boldsymbol{p}_1 - \boldsymbol{p}_2$ is the relative momentum and $\boldsymbol{p} = \hbar\boldsymbol{k}$. The energy eigenvalue has been written as $E_n = \hbar^2 k_0^2/M$, with n also used to label the incident momentum

vector for scattering and the spin and isospin quantum numbers. The wave function $\psi_n(\boldsymbol{k})$ is simply the Fourier transform of $\psi_n(\boldsymbol{r})$

$$\psi_n(\boldsymbol{k}) = (2\pi)^{-\frac{3}{2}} \int d\boldsymbol{r}\, e^{i\boldsymbol{k}\cdot\boldsymbol{r}} \psi_n(\boldsymbol{r}), \tag{2.3}$$

and the potential matrix elements in momentum space are related to the nonlocal operator $V(\boldsymbol{r}|\boldsymbol{r}')$ by

$$V(\boldsymbol{k}|\boldsymbol{k}') = (2\pi)^{-3} \int d\boldsymbol{r}\, d\boldsymbol{r}'\, e^{-i\boldsymbol{k}\cdot\boldsymbol{r}} V(\boldsymbol{r}|\boldsymbol{r}') e^{i\boldsymbol{k}'\cdot\boldsymbol{r}'}. \tag{2.4}$$

The next step is to introduce a partial wave decomposition of the wave function

$$\psi_n(k) = \sum_{\alpha LL'M} i^{L-L'} \psi^{\alpha}_{LL'}(k) Y_{LM_L}(\boldsymbol{k}_0) \langle LSM_L M_S | JM \rangle \mathscr{Y}^{JM}_{L'S}(\hat{\boldsymbol{k}}) | TT_3 \rangle. \tag{2.5}$$

The wave function is decomposed into normalized eigenstates of the total angular momentum J, the total spin S, and the total orbital angular momentum L of the two nucleons. These eigenstates are formed using the Clebsch-Gordan coefficient $\langle LSM_L M_S | JM \rangle$:

$$\mathscr{Y}^{JM}_{LS}(\boldsymbol{k}) = \sum_{M_L M_S} \langle LSM_L M_S | JM \rangle Y_{LM_L}(\boldsymbol{k}) | SM_S \rangle. \tag{2.6}$$

Throughout this paper α denotes the quantum numbers JST.

The corresponding decomposition of the potential is

$$V(\boldsymbol{k}|\boldsymbol{k}') = \frac{2}{\pi} \frac{\hbar^2}{M} \sum i^{L-L'} V^{\alpha}_{LL'}(k|k') \mathscr{Y}^{JM}_{LS}(\hat{\boldsymbol{k}}) \mathscr{Y}^{JM+}_{LS}(\hat{\boldsymbol{k}}) P_T, \tag{2.7}$$

where $V(\boldsymbol{k}|\boldsymbol{k}')$ is an operator in spin and isospin space and P_T is an isospin projection operator. Eq. (2.7) represents the most general potential that conserves total angular momentum, parity and isospin. The potential satisfies time reversal invariance if $V_{LL'}(k|k') = V_{L'L}(k'|k)$. The sum is restricted to those quantum numbers $\alpha LL'$ of two-nucleon states that are allowed by the Pauli principle, i.e. states having $S+L+T$ equal to an odd integer. For triplet states the orbital angular momenta $L = J \pm 1$ can be coupled by a tensor or noncentral potential; thus both L and L' labels appear on $V_{LL'}$ and $\psi_{LL'}$.

Let us now consider the scattering and bound state problems formulated in momentum space.

2.2. THE SCATTERING PROBLEM

In momentum space the Schrödinger equation for standing waves is

$$\psi_n(\boldsymbol{k}) = \delta(\boldsymbol{k}-\boldsymbol{k}_0)|SM_S\rangle|TT_3\rangle - \frac{M}{\hbar^2} \frac{\mathrm{P}}{k^2-k_0^2} \int d\boldsymbol{k}'\, V(\boldsymbol{k}|\boldsymbol{k}') \psi_n(\boldsymbol{k}'). \tag{2.8}$$

The symbol P means principal value. The incoming momentum vector $\hbar \boldsymbol{k}_0$ and incident spin-isospin state are labeled by n.

Instead of solving directly for the wave function, it is convenient to introduce a reaction matrix defined by $R\phi_n = V\psi_n$, where ϕ_n is a plane wave. The result is the Lippmann-Schwinger equation

$$R(\boldsymbol{k}|\boldsymbol{k}_0) = V(\boldsymbol{k}|\boldsymbol{k}_0) - \frac{M}{\hbar^2} \mathrm{P} \int \frac{\mathrm{d}\boldsymbol{k}' V(\boldsymbol{k}|\boldsymbol{k}') R(\boldsymbol{k}'|\boldsymbol{k}_0)}{k'^2 - k_0^2}. \tag{2.9}$$

It is easy to construct the wave function and phase shifts from the R-matrix, once a partial wave decomposition is used. The result is the one-dimensional, coupled-channels, Lippman-Schwinger equation

$$R^{\alpha}_{LL'}(k|k_0) = V^{\alpha}_{LL'}(k|k_0) - \frac{2}{\pi} \mathrm{P} \sum_l \int_0^{\infty} \frac{\mathrm{d}k' k'^2 V_{Ll}(k|k') R_{lL'}(k'|k_0)}{k'^2 - k_0^2}. \tag{2.10}$$

The channels are αL and $\alpha L'$, which can be coupled by a tensor force. In triplet states the orbital angular momenta $L = J \pm 1$ are coupled. For numerical work it is convenient that only real quantities arise in (2.10). The corresponding wave function in momentum space is

$$\psi^{\alpha}_{LL'}(k) = \frac{1}{k^2} \delta(k - k_0) \delta_{LL'} - \frac{2}{\pi} \mathrm{P} \frac{R_{LL'}(k|k_0)}{k^2 - k_0^2}. \tag{2.11}$$

Using (2.3), the configuration space scattering wave function is

$$\psi^{\alpha}_{LL'}(r) = j_L(k_0 r) \delta_{LL'} - \frac{2}{\pi} \int_0^{\infty} \frac{\mathrm{d}k' k'^2 j_{L'}(k' r) R_{L'L}(k'|k_0)}{k'^2 - k_0^2}. \tag{2.12}$$

A contour integration of (2.12) can be used to find the asymptotic wave function

$$k_0 r \psi^{\alpha}_{LL'}(r) \underset{r \to \infty}{\to} j_L(k_0 r) \delta_{LL'} - k_0 R_{L'L}(k_0) n_{L'}(k_0 r), \tag{2.13}$$

where j_L and n_L are the regular and irregular spherical Bessel functions, respectively. It is the on-energy-shell matrix element $R_{LL'}(k_0) \equiv R_{LL'}(k_0|k_0)$ that determines the asymptotic wave function. This important property follows from the occurrence of the energy conserving singularity at $k'^2 = k_0^2$ in the integrand of (2.13).

In the Blatt-Biedenharn convention the eigenphases for the coupled channels are determined from the on-energy-shell R-matrix

$$\begin{aligned} \mathrm{tg}\, \delta^{\alpha}_{J \pm 1}(k_0) &= -\tfrac{1}{2} k_0 \left[R^{\alpha}_{J-1,J-1} + R^{\alpha}_{J+1,J+1} \mp \frac{(R^{\alpha}_{J-1,J-1} - R^{\alpha}_{J+1,J+1})}{\cos 2\varepsilon^{\alpha}_J} \right], \\ \mathrm{tg}\, 2\varepsilon^{\alpha}_J(k_0) &= \frac{2R^{\alpha}_{J-1,J+1}}{R^{\alpha}_{J-1,J-1} - R^{\alpha}_{J+1,J+1}}. \end{aligned} \tag{2.14}$$

Here $\delta^{\alpha}_{J \pm 1}$ are the eigenphase shifts and ε^{α}_J is the mixing parameter, which is a measure

of the coupling produced by the tensor interaction. For uncoupled channels, corresponding to $\varepsilon_J \to 0$, the standard result is obtained

$$\operatorname{tg} \delta_L^\alpha(k_0) = -k_0 R_L^\alpha(k_0). \tag{2.15}$$

The main feature of using momentum space is that one can obtain both the phase shifts and the wave function from eqs. (2.11)–(2.15), once the Lippmann-Schwinger equation is solved for the R-matrix. This procedure is particularly useful for nonlocal potentials.

2.3. MATRIX INVERSION SOLUTION

One way of solving the Lippmann-Schwinger equation is to use the Born series. However, in channels having a bound state ($^3S_1 + {}^3D_1$) or a resonance it is well known that the Born series diverges[4]). Also, for the case of a virtual state ($^1S_0$) and for very strong potentials the Born series is known to converge slowly, if at all. Two methods that can be used have been suggested by Weinberg and by Noyes and Kowalski [4]).

A third and even simpler method is to use matrix inversion. Let us first consider (2.10) for uncoupled channels ($L = L'$) and add a zero term to replace the principal value condition by a smooth integrand

$$R_L^\alpha(k|k_0) = V_L^\alpha(k|k_0) - \frac{2}{\pi}\int_0^\infty \frac{\mathrm{d}k'[k'^2 V_L^\alpha(k|k')R_L^\alpha(k'|k_0) - k_0^2 V_L^\alpha(k|k_0)R_L^\alpha(k_0|k_0)]}{k'^2 - k_0^2}. \tag{2.16}$$

The integrand has a finite limit even for $k' = k_0$; however, we wish to avoid such points. Our goal is to solve eq. (2.16) numerically without having any points at which $k' = k_0$. At the same time we need to find the R-matrix both on and off the energy shell.

These quantities can be easily found by introducing an N-point integration formula

$$\int_0^\infty \mathrm{d}k F(k) = \sum_{j=1}^{N} F(k_j)\omega_j, \tag{2.17}$$

where we have preferred to take k_j and ω_j to be either Laguerre or Gaussian integration points and weights. For Gaussian integration the mapping $k = \operatorname{tg}\frac{1}{2}\pi x$ was used. Gaussian integration is used for potentials having a relatively slow fall-off in momentum space.

All of the N integration points, $k_1 \ldots k_N$, are required to be unequal to k_0. If we call k_0 the $N+1$ point ($k_0 \equiv k_{N+1}$), then eq. (2.16) can be rewritten as

$$V_L^\alpha(k_i|k_{N+1}) = \sum_{j=1}^{N+1} F_L^\alpha(k_i|k_j)R_L^\alpha(k_j|k_{N+1}). \tag{2.18}$$

The matrix F_L is simply

$$F_L^\alpha(k_i|k_j) = \delta_{ij} + \omega_j' V_L^\alpha(k_i|k_j), \tag{2.19}$$

where ω_j' is defined by

$$\omega_j' = \begin{cases} \frac{2}{\pi} \frac{k_j^2 \omega_j}{k_j^2 - k_0^2} & \text{for } j \leqq N, \\ -\frac{2}{\pi} \sum_{m=1}^{N} \frac{\omega_m}{k_m^2 - k_0^2} k_0^2 & \text{for } j = N+1. \end{cases} \tag{2.20}$$

The matrix F is nonsingular since k_{N+1} is distinct from the grid points; it can therefore be inverted to yield the R-matrix both on and off the energy shell

$$R^{\alpha}(k_i|k_{N+1}) = \sum_{j=1}^{N+1} F_L^{-1}(k_i|k_j) V_L^{\alpha}(k_j|k_{N+1}). \tag{2.21}$$

The extension to coupled channels is straightforward. One simply combines the points and the label L to form a larger $(2N+2)\times(2N+2)$ dimensional matrix

$$V^{\alpha}(i,j) = \sum_{j=1}^{2N+2} F^{\alpha}(i,j) R^{\alpha}(j,j). \tag{2.22}$$

Here the i, j, and j labels include both the points $k_1, \ldots k_{N+1}$ and the L-value. For example, for $L = J-1$ we take the $1 \leqq i \leqq N+1$ points as $k_1, \ldots k_{N+1}$. For $L = J+1$, the label i ranges as $N+2 \leqq i \leqq 2N+2$ with identical k-values, $k_1, \ldots k_{N+1} \equiv k_{N+2}, \ldots k_{2N+2}$.

2.4. NUMERICAL TEST OF MATRIX INVERSION

To test the accuracy of the matrix inversion solution, we used two potentials. One is an S-wave, square well attraction with a short-range repulsion; the other is the Yukawa-core Reid potential [1]). The square well case has a 50 MeV attraction of range 2.5 fm plus a constant repulsive core of 100 GeV strength with a range of 0.4 fm. This potential is very strong and yields a deep bound state. Its phase shifts are known analytically. Therefore, it provides us with a stringent test of matrix inversion in momentum space.

TABLE 1

Comparison of matrix inversion $^1S_0$ phase shifts and analytic $^1S_0$ phase shifts for a finite-core-plus-plus-square-well potential

Lab energy (MeV)	$N = 15$	$N = 25$	Analytic
2.00	2.61207	2.61298	2.61284
20.75	1.61056	1.62751	1.62413
100.00	0.50375	0.50486	0.50385
140.27	0.25500	0.25821	0.25821
200.00	0.04529	0.04903	0.04984
300.00	−0.10612	−0.10831	−0.10694

Laguerre integration points are used. All phase shifts are in radians.

The Reid Yukawa-core potential [1]) is also considered because it is another potential having large matrix elements for which the phase shifts are known accurately. The results of these test calculation appear in tables 1 and 2. The $^3S_1 + {}^3D_1$ eigenphase shifts were obtained with the same precision.

TABLE 2

Comparison of matrix inversion $^1S_0$ phase shifts and $^1S_0$ phase shift for the Reid Yukawa-core potential

Lab energy (MeV)	$N = 16$	$N = 24$	Reid
24	0.86182	0.86071	0.86055
48	0.68560	0.68466	0.68459
96	0.44111	0.44080	0.44019
144	0.26395	0.26310	0.26303
208	0.08135	0.08040	0.08033
352	−0.21511	−0.21630	−0.21638

The Reid phase shifts given here do not include the Coulomb interaction and are obtained from tables 2 and 18 of Reid's thesis [1]). Gaussian integration routines are used. All phase shifts are in radians.

Tables 1 and 2 demonstrate that matrix inversion provides an excellent means of solving the Schrödinger equation in the scattering problem for finite potentials. The matrix inversion method gives excellent precision even when the potential has large matrix elements, i.e. a 100 GeV core can be handled. For the Reid $^1S_0$ Yukawa-core potential, the computer time required is only 11 seconds for seven energies and 24 grid points on the IBM 7090. The precision obtained is better than 0.001 rad for the Reid $^1S_0$ soft-core potential with 24 Gaussian points. The precision for the square well case is 0.003 rad for 25 Laguerre points. Furthermore, the calculated phase shifts, after some small oscillations, are stable as one increases the number of grid points. Stability with increasing number of grid points is an important requirement for the method to be reliable. For most cases 16 points provides sufficient accuracy.

2.5. THE BOUND STATE

The bound state energy and wave function for general nonlocal potentials can also be found by matrix inversion in momentum space. The energy is now negative, $E_D = -(\hbar^2/M)\, k_D^2$, and the incident plane wave part of eqs. (2.8)–(2.22) must be deleted. We have to solve

$$\sum_{i=1}^{2N} F_D(i,j)\psi(j) = 0, \tag{2.23}$$

with F_D given by

$$F_D(i,j) = \delta_{ij} + \frac{2}{\pi}\frac{k_j^2 \omega_j}{k_j^2 + k_D^2} V(i|j). \tag{2.24}$$

As before, the indices i and j incorporate both the orbital angular momentum L, and the grid points $k_1, \ldots k_N$. Eq. (2.23) involves a $2N \times 2N$ matrix problem of standard homogeneous form, $F\psi = 0$. The binding energy produced by a given potential is found by varying k_D until the determinant det F is zero. Knowing the binding energy, one can solve (2.23) for the wave function, $\psi(j)$. The momentum space wave function of the deuteron is obtained this way and used to calculate the D-state probability quoted in table 6 of sect. 4.

Direct matrix inversion thus proves to be a valid means of solving the two-nucleon problem for general finite potentials. The next step is to extend this technique to the nuclear matter problem.

3. Solution of the Brueckner equation for nuclear matter

To study various aspects of the two-nucleon interaction and their influence on nuclear binding energies, one must first have a valid technique for calculating binding energies. The linked-cluster Rayleigh-Schrödinger, or Goldstone expansion, for the ground state energy provides the required technique [7]). To remedy the lack of convergence associated with a hard-core repulsion, Brueckner [10]) summed selected terms of this perturbation expansion to define the reaction matrix G. The ground state energy of the many-body system is then obtained from the finite G-matrix.

The G-matrix plays the role of an effective interaction for two particles in the nuclear medium. It is finite even for singular potentials, in much the same way that the R-matrix for free scattering is finite for singular potentials. In fact, the equation that defines G, the Brueckner equation, resembles the Lippmann-Schwinger equation for R. As was true for the R-matrix, one can use matrix inversion in momentum space to calculate the G-matrix for infinite nuclear matter. Later (sect. 5) this technique is used to study the saturation properties of nonlocal potentials.

It is the consideration of nonlocal potentials that leads us to use matrix inversion instead of alternate methods For example, the reference spectrum method is best suited for the case of local potentials, since only standard second-order differential equations are involved [11]). However, for general nonlocal potentials it is simpler to use the direct matrix inversion solution that will be discussed.

3.1. NUCLEAR MATTER AND THE BRUECKNER G-MATRIX

Nuclear matter is defined to be an infinite system consisting of an equal number of protons and neutrons The Coulomb interaction is absent and the number of particles, A, approaches infinity. The particle density ρ is constant and the single-particle wave functions, or orbitals, are taken to be plane waves. In configuration space the single-particle orbitals, $\phi_\mu(r_i)$, are given by

$$\phi_\mu(r_i) = \langle r_i|\mu\rangle = \frac{\exp i\boldsymbol{k}_\mu \cdot \boldsymbol{r}_i}{\Omega^{\frac{1}{2}}} |s_\mu t_\mu\rangle, \tag{3.1}$$

where s_μ labels the spin state of the nucleon, and t_μ is the isospin label. The nucleons are in the volume Ω, which is used in (3.1) to normalize the single-particle orbitals. For an infinite system, both A and Ω approach infinity, while the particle density $\rho = A/\Omega$ remains finite.

The ground state of nuclear matter is simply a properly antisymmetrized product of orbitals with all levels filled, according to the Pauli principle, up to a maximum level specified by k_F, the Fermi momentum. For this state, the total kinetic energy is $\langle T\rangle = \frac{3}{5}\varepsilon_F A$. The Fermi energy is given by $\varepsilon_F = (\hbar^2/2M)k_F^2$ and the particle density is $\rho = 2k_F^3/3\pi^2$.

The main goal of nuclear matter calculations is to determine the saturation curve, i.e. binding energy per nucleon as a function of density. The equilibrium binding energy and density are determined by finding a minimum in the saturation curve. The basic saturation condition placed on a potential by nuclear matter is that the correct binding energy and density be obtained. This correct binding energy, as extracted from the volume term of the semi-empirical mass formula, is $E/A = -15.8$ MeV/A. The equilibrium density of nuclear matter corresponds to a Fermi momentum of $k_F = 1.36$ fm^{-1}. This value results from a study of the interior density of finite nuclei after Coulomb and surface effects have been accounted for [7]).

To calculate these saturation properties, one must first solve the Brueckner equation for the G-matrix

$$G(\omega) = V + V\frac{Q}{\omega - h_0}G(\omega). \tag{3.2}$$

Here Q, the Pauli principle projection operator, projects out states with two nucleons above the Fermi sea:

$$Q|\alpha\beta\rangle = \begin{cases} 1 & \text{for } \alpha \text{ and } \beta \text{ above } \varepsilon_F \\ 0 & \text{for } \alpha \text{ and } \beta \text{ at or below } \varepsilon_F. \end{cases} \tag{3.3}$$

The Hamiltonian h_0 includes a kinetic energy plus a single-particle potential. Acting on product states it gives

$$h_0|\alpha\beta\rangle = (\varepsilon_\alpha + \varepsilon_\beta)|\alpha\beta\rangle, \tag{3.4}$$

where the single-particle energies ε_α are simply $\varepsilon_\alpha = (\alpha|(p^2/2M) + U|\alpha)$. The single-particle potential is itself determined by the interaction of each nucleon with all others in the Fermi sea; for nucleons below the Fermi level it is defined by

$$\langle\mu|U|\mu\rangle = U(k_\mu) = \sum_{\nu<F}\langle\mu\nu|G(\varepsilon_\mu+\varepsilon_\nu)|\mu\nu - \nu\mu\rangle, \qquad \text{for} \quad \mu \leqq F, \tag{3.5}$$

which includes both direct and exchange terms. The starting energy ω is chosen to be $\omega = \varepsilon_\mu + \varepsilon_\nu$, according to the Bethe-Brandow-Petshek (BBP) theorem [11]). This definition of U is based on the requirement that U cancels the bubble, or self-energy insertions, that occur on hole lines in higher-order terms of the Brueckner-Goldstone expansion [11]).

A clear choice of single-particle potential for nucleons above the Fermi sea is not available. The current thinking on that problem is to use a zero single-particle potential above the Fermi sea; this choice has been used by Sprung and by Kallio and Day [12]). It rests on the Bethe and Rajaraman [11]) result that the relevant three-body diagrams sum to only – 1 MeV and therefore no appreciable single-particle potential is required for cancellation. In this paper, a zero single-particle potential above the Fermi sea is used .

Recently, Baranger, Kao and Depp [13]) have examined the problem of defining the single-particle potential just above the Fermi sea, i.e. for $k_F < k \leqq 2k_F$. That problem involves improving the three-body diagram calculation by including attractive tail and tensor force effects. A recent paper by Brown and Green [14]) indicates that long-range three-body forces may also be significant. Clearly, future work on nuclear matter and finite nuclei should include such effects, but they are beyond the scope of this paper.

Once eqs. (3.2)–(3.5) are used to find the G-matrix, the binding energy can be evaluated from

$$\begin{aligned} E &= \sum_{\mu<F} \langle \mu | \frac{p^2}{2M} | \mu \rangle + \tfrac{1}{2} \sum_{\mu,\nu \leqq F} \langle \mu\nu | G(\varepsilon_\mu + \varepsilon_\nu) | \mu\nu - \nu\mu \rangle \\ &= \sum_{\mu \leqq F} (\varepsilon_\mu - \tfrac{1}{2} U_\mu). \end{aligned} \tag{3.6}$$

Here it is seen that G plays the role of an effective two-body interaction in the nuclear medium.

We can now write (3.2) explicitly by introducing the relative and c.m. momenta $2\boldsymbol{k}_{\mu\nu} = \boldsymbol{k}_\mu - \boldsymbol{k}_\nu$, and $2\boldsymbol{K}_{\mu\nu} = \boldsymbol{k}_\mu + \boldsymbol{k}_\nu$ (We will often omit the state subscripts.) The discrete sums now become continuous integrations, i.e. $\sum_\mu \to \Omega(2\pi)^{-3} \int_{k_\mu \leqq k_F} \mathrm{d}k_\mu$. In our discussion the starting energy, ω, will always be evaluated on the energy shell $\omega \equiv E(\boldsymbol{k}_0, \boldsymbol{K})$, where $E(\boldsymbol{k}_0, \boldsymbol{K})$ is defined in (3.8). The G-matrix equation is then

$$G(K\boldsymbol{k}, \boldsymbol{k}_0) = V(\boldsymbol{k}, \boldsymbol{k}_0) - \int \frac{\mathrm{d}\boldsymbol{k}' V(\boldsymbol{k}|\boldsymbol{k}') Q(\boldsymbol{k}', \boldsymbol{K}) G(\boldsymbol{K}|\boldsymbol{k}', \boldsymbol{k}_0)}{E(\boldsymbol{k}', \boldsymbol{K}) - E(\boldsymbol{k}_0, \boldsymbol{K})}, \tag{3.7}$$

where $Q(\boldsymbol{k}', \boldsymbol{K})$ satisfies the Pauli principle condition $Q(\boldsymbol{k}', \boldsymbol{K}) = 1$ for $|\boldsymbol{k}' + \boldsymbol{K}| > k_F$ and $Q(\boldsymbol{k}', \boldsymbol{K}) = 0$ for $|\boldsymbol{k}' \pm \boldsymbol{K}| \leqq k_F$. In nuclear matter, the single-particle energies are functions of $|\boldsymbol{k}_\alpha|$, $\varepsilon(k_\alpha) = (\hbar^2/2M)k_\alpha^2 + U(|\boldsymbol{k}_\alpha|)$. Therefore, the above energy denominator is given by

$$\begin{aligned} E(\boldsymbol{k}', \boldsymbol{K}) - E(\boldsymbol{k}_0, \boldsymbol{K}) = \frac{\hbar^2}{M}(k'^2 - k_0^2) + U(|\boldsymbol{K} + \boldsymbol{k}'|) + U(|\boldsymbol{K} - \boldsymbol{k}'|) \\ - U(|\boldsymbol{K} + \boldsymbol{k}_0|) - U(|\boldsymbol{K} - \boldsymbol{k}_0|). \end{aligned} \tag{3.8}$$

Note that (3.8) depends on the angles between $\boldsymbol{K}$ and $\boldsymbol{k}'$, and between $\boldsymbol{K}$ and $\boldsymbol{k}_0$. The Pauli operator $Q(\boldsymbol{k}', \boldsymbol{K})$ also depends on the angle between $\boldsymbol{K}$ and $\boldsymbol{k}'$. The above

dependence on angles causes Q to couple states with different relative angular momentum J. A partial wave decomposition of (3.7) is therefore rather complicated and further simplifications are needed.

3.2. THE ANGLE AVERAGED PAULI OPERATOR AND THE EFFECTIVE MASS APPROXIMATIONS

The angle averaged Pauli operator and effective mass approximations are used to simplify eq. (3.7) by eliminating the awkward angle dependence [12, 15]). These approximations were examined by Irwin in his Cornell thesis, where he shows them to be valid; for example, he finds the effect of J-coupling on nuclear binding energies to be less than 0.1 MeV/A [ref. [15])].

In the angle average approximation, one replaces the exact Q-operator, $Q(\boldsymbol{k}', \boldsymbol{K})$, by its average over all angles for fixed $|\boldsymbol{k}'|$ and $|\boldsymbol{K}|$. The angle averaged Q-operator, $\bar{Q}(k', K)$ is

$$\begin{aligned} \bar{Q}(k', K) &= 0 && \text{for} \quad k' \leqq \sqrt{k_F^2 - K^2}, \\ &= 1 && \text{for} \quad k' \geqq k_F + K, \\ &= \frac{K^2 + k'^2 - k_F^2}{2Kk'} && \text{for} \quad \sqrt{k_F^2 - K^2} < k' \leqq k_F + K. \end{aligned} \tag{3.9}$$

Note that $\bar{Q}(k', K)$ has discontinuous derivatives at $k' = (k_F^2 - K^2)^{\frac{1}{2}}$ and $k' = k_F + K$.

Using the angle averaged Q-operator, one can eliminate one source of angle dependence. The other remaining dependence on angle is handled by the effective mass approximation. The single-particle energies are assumed to have the quadratic form

$$\begin{aligned} \varepsilon(k_\alpha) &= \frac{\hbar^2 k_\alpha^2}{2M^*} - U_0 && \text{for} \quad k_\alpha \leqq k_F \\ &= \frac{\hbar^2 k_\alpha^2}{2M} && \text{for} \quad k_\alpha > k_F, \end{aligned} \tag{3.10}$$

where M^* is called the effective mass. With this choice of single-particle spectrum, the angular dependence disappears from $E(\boldsymbol{k}, \boldsymbol{K})$ and $E(\boldsymbol{k}_0, \boldsymbol{K})$. The resulting expressions are

$$\begin{aligned} E(k', K) &= \frac{\hbar^2}{M}(K^2 + k'^2) = \frac{\hbar^2}{M} E_>, \\ E(k_0, K) &= \frac{\hbar^2}{M^*}(K^2 + k_0^2) - 2U_0 = \frac{\hbar^2}{M} E_<. \end{aligned} \tag{3.11}$$

The symbols $E_<$ and $E_>$ stand for the energies of two particles below the Fermi sea and of two particles above the Fermi sea, respectively. Note that the single-particle potential for $k > k_F$ is taken to be zero as previously discussed.

The choice of the hole spectrum, as given by (3.10) presents a self-consistency

problem since (3.5) relates U and G; the determination of G, however, depends on the choice of U. Therefore, the calculation of U by (3.5) should reproduce the U used to calculate G. To make U self-consistent in the effective mass approximation, the initial values of M^* and U_0 are chosen to calculate G; then from G new values of M^* and U_0 are obtained using (3.5) and (3.10). This procedure continues until M^* and U_0 change very little; with reasonable starting values for M^* and U_0 two or three cycles suffice to achieve self-consistency.

The calculation of binding energies and self-consistent single-particle energies requires that we solve the Brueckner equation. Even after removal of the above angular dependence, (3.7) is a three-dimensional integral equation. A partial-wave decomposition will now be used to reduce (3.7) to a set of one-dimensional integral equations, just as in the case of the Lippmann-Schwinger equation.

3.3. PARTIAL-WAVE DECOMPOSITION OF THE BRUECKNER EQUATION

With the angle-averaged Q and effective mass approximations, the Brueckner equation becomes

$$G(K|\boldsymbol{k}, \boldsymbol{k}_0) = V(\boldsymbol{k}|\boldsymbol{k}_0) - \int \frac{\mathrm{d}\boldsymbol{k}' V(\boldsymbol{k}|\boldsymbol{k}') \bar{Q}(k', K) G(K|\boldsymbol{k}', \boldsymbol{k}_0)}{E(k, K) - E(k_0, K)}. \tag{3.12}$$

Neither $\bar{Q}$ nor the energy denominators in (3.10) now depend on the direction of $\boldsymbol{K}$. Therefore, G is a function of $\boldsymbol{k}$, $\boldsymbol{k}_0$ and $|\boldsymbol{K}|$.

To reduce (3.12) to a set of one-dimensional integral equations the standard partial-wave decomposition can be used

$$G(K|\boldsymbol{k}, \boldsymbol{k}_0) = \frac{2}{\pi} \frac{\hbar^2}{M} \sum_{\substack{\alpha LL' \\ M}} i^{L-L'} G^{\alpha}_{LL'}(K|k, k_0) \mathscr{Y}^{JM}_{LS}(\hat{\boldsymbol{k}}) \mathscr{Y}^{JM+}_{L'S}(\hat{\boldsymbol{k}}_0) P_T. \tag{3.13}$$

The resulting one-dimensional coupled-channels Brueckner equation is

$$G^{\alpha}_{LL'}(K|k, k_0) = V^{\alpha}_{LL'}(k|k_0) - \frac{2}{\pi} \sum_l \int_0^{\infty} \frac{\mathrm{d}k' k'^2 \bar{Q}(k', K) V^{\alpha}_{Ll}(k|k') G^{\alpha}_{lL'}(K|k', k_0)}{E_>(k', K) - E_<(k_0, K)}. \tag{3.14}$$

As before, α denotes JS and T. Eq. (3.14) differs from the Lippmann-Schwinger equation in two important ways. First the energy denominators include single-particle potentials that arise from the presence of the other nucleons – this is simply a recognition of the many-nucleon medium in which the pair is moving. Secondly, the nuclear medium produces the Pauli exclusion effect as recorded in $\bar{Q}$. Because of $\bar{Q}$, the integrand in (3.14) does not have a singularity, which causes the healing of the two-nucleon wave function in the nuclear medium. The significance and quantitative measure of healing will be discussed in detail later (sect. 5).

The nonsingular character of the integrand of (3.14) makes it completely suitable for a matrix inversion method. We spare the reader the details since it is obvious that only slight changes in the definition of F [eq. (2.19)] are required to make the discussion of sect. 2 applicable to (3.14).

To test the accuracy of the direct matrix-inversion technique, we calculated the G matrix elements for a very strong $^1S_0$ separable potential. The potential chosen has the form

$$V_{00}(k|k;) = -g_0(k)g_0(k'),$$
$$g_0(k) = \alpha/(k^2+a^2), \tag{3.15}$$

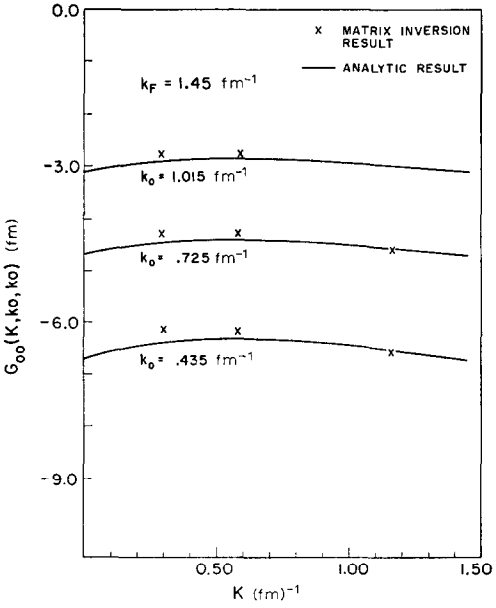

Fig. 1. The diagonal G matrix elements for a strong separable potential (3.15). The matrix inversion result using 15 Laguerre points is compared to the analytic G-matrix (3.16). Here $M^*/M = 0.8$ and $U_0 = 80$ MeV were used.

with $\alpha = 3.6\,\mathrm{fm}^{-\frac{3}{2}}$ and $a = 1.2\,\mathrm{fm}^{-1}$. The analytic G-matrix for the above potential (in the angle averaged $\bar{Q}$ and effective mass approximations) is given by

$$G^{\alpha}_{00}(K|k, k_0) = -g_0(k)g_0(k_0)\left[1-\frac{2}{\pi}\int_0^{\infty}\frac{\mathrm{d}k'k'^2 g_0^2(k')\bar{Q}(k', K)}{E_<(k', K)-E_<(k_0, K)}\right]^{-1}. \tag{3.16}$$

The integral in (3.16) is given analytically in ref. [16]).

Fig. 1 shows some of the G matrix elements obtained by matrix inversion with 15 Laguerre points. These results are compared to the analytic values, eq. (3.16). Self-consistency is considered later; here reasonable values for M^* and U_0 were used. Accuracy of the direct matrix inversion method is seen to improve with increasing c.m. momentum K. The accuracy at higher c.m. momenta improves because the discontinuities in $(\partial/\partial k')\bar{Q}(k', K)$ (at $k' = (k_F^2-K^2)^{\frac{1}{2}}$ and at $k' = k_F+K$) decrease in magnitude with increasing K. These discontinuities introduce only a small impreci-

sion in the numerical matrix inversion. Because an average c.m. momentum is used later, the imprecision at small K leads to negligible errors in the total binding energy.

3.4. CALCULATION OF THE SINGLE-PARTICLE SPECTRUM

The next step in obtaining nuclear binding energies is to calculate the self-consistent single-particle spectrum. According to the prescription of BBP the single-particle potential operator U should satisfy (3.5). Using (3.5) and (3.13), one finds the following expression for the single-particle potential for $k_\mu \leqq k_F$

$$U(k_\mu) = \frac{4}{\pi}\frac{\hbar^2}{M}\frac{1}{k_\mu}\sum_{(\alpha L)}(2J+1)(2T+1)\left\{\left[\int_0^{\frac{1}{2}(k_F-k_\mu)} dk_0\, k_0 \int_{k_\mu-k_0}^{k_\mu+k_0} dK K + \int_{\frac{1}{2}(k_F-k_\mu)}^{\frac{1}{2}(k_F+k_\mu)} dk_0\, k_0 \int_{|k_\mu-k_0|}^{[\frac{1}{2}(k_F^2+k_\mu^2)-k_0^2]^{\frac{1}{2}}} dK K\right] G^\alpha_{LL}(K|k_0, k_0)\right\}. \tag{3.17}$$

Details of the steps leading to (3.17) are given in refs. [15,16]). (One must take into account the Pauli principle conditions $k_\mu \leqq k_F$ and $k_\nu \leqq k_F$ and use the proper transformation of variables.)

Eq. (3.17) is a double integral. To reduce the dimension of the integral and the number of G matrix elements needed to compute U, we make the further approximation that

$$G^\alpha_{LL}(K, k_0, k_0) \approx G^\alpha_{LL}(K_{av}|k_0, k_0). \tag{3.18}$$

The average c.m. momentum, K_{av}, is chosen to be the value of K for two particles in the Fermi sea, with the constraint that one of the particles has momentum k_μ and their relative momentum has magnitude k_0. The resulting average c.m. momentum is given by

$$K_{av}^2 = \begin{cases} k_\mu^2 + k_0^2, & \text{for } 2k_0 \leqq k_F - k_\mu \\ k_\mu^2 + k_0^2 - \frac{1}{4}(2k_0 + k_\mu - k_F)(2k_0 + k_\mu + k_F), & \text{for } k_F - k_\mu \leqq 2k_0 \leqq k_F + k_\mu. \end{cases} \tag{3.19}$$

With the approximations (3.18) and (3.19), the expression for $U(k_\mu)$ simplifies to

$$U(k_\mu) = 8\frac{\hbar^2}{M}\sum_{\alpha L}(2J+1)(2J+1)\left\{\left[\int_0^{\frac{1}{2}(k_F-k_\mu)} dk_0\, k_0^2 + \frac{1}{2k_\mu}\int_{\frac{1}{2}(k_F-k_\mu)}^{\frac{1}{2}(k_F+k_\mu)} dk_0\, k_0^2\left(\tfrac{1}{4}(k_F^2-k_\mu^2) - k_0(k_0-k_\mu)\right)\right] G^\alpha_{LL}(K_{av}, k_0, k_0)\right\}. \tag{3.20}$$

Eq. (3.20) is evaluated numerically by Simpson's rule. A ten-point Simpson's rule sufficies to evaluate (3.20). If 20 points are used, the values of $U(k_\mu)$ change only in the fourth or fifth significant figure.

The average c.m. approximation is valid only if G has a weak dependence on K. Indeed, it is found that $G(K|k_0, k_0)$ varies little with K, i.e. by less than 10 % for a given k_0. This property can be verified by inspection of fig. 1.

The precision of the single-particle potential obtained using the matrix-inversion method, along with the average c.m. momentum approximation, can be determined by using the previously mentioned separable potential. In fig. 2 the single-particle

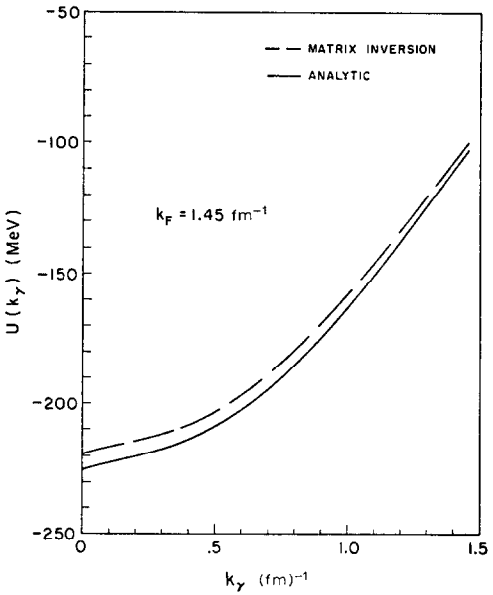

Fig. 2. The single-particle potential for a strong separable potential. The matrix inversion values are compared to the analytic result, which is obtained using (3.16) and (3.17). Here $M^*/M = 0.8$ and $U_0 = 80$ MeV were used.

spectrum obtained by matrix inversion is compared to that obtained using the exact G-matrix, eq. (3.16). The analytic calculation does not involve the average c.m. momentum approximation, but rather includes both integrations in (3.17). All calculations are for $k_F = 1.45\ \text{fm}^{-1}$, $M^*/M = 0.8$, and $U_0 = 80$ MeV.

The deviation of the analytic single-particle potential from those obtained by matrix inversion with the average c.m. approximation range from 2 % to 4 % for 15 Laguerre point matrix inversion. However these test calculations are for an extremely strong potential and much better accuracy is found for realistic potentials. In addition, a 2–4 % error in the single-particle spectrum has only a very small effect on the calculation of nuclear binding energies. Therefore, the use of matrix inversion along with the average c.m. approximation proves to be a sufficiently precise method for calculating the binding energy of nuclear matter.

3.5. CALCULATION OF THE BINDING ENERGY OF NUCLEAR MATTER

The total ground state energy of nuclear matter is given by eq. (3.6). Application of the partial wave expansion yields

$$\frac{E}{A} = \tfrac{3}{5}\varepsilon_F + \frac{3}{\pi^2}\frac{\hbar^2}{M}\frac{1}{k_F^3}\sum_{(\alpha L)}(2J+1)(2T+1)\left\{4\pi\int_0^{k_F} dk_0\, k_0^2\left[\int_0^{k_F-k_0} dK K^2 + 2\pi\int_{k_F-k_0}^{\sqrt{k_F^2-k_0^2}} dK K^2\,\frac{k_F^2-K^2-k_0^2}{k_0 K}\right] G^{\alpha}_{LL}(K|k_0, k_0)\right\}. \quad (3.21)$$

The integration limits are determined by the overlap of the two Fermi spheres. We must satisfy $|\boldsymbol{k}_0 \pm \boldsymbol{K}| \leqq k_F$, where $\boldsymbol{k}_0$ and $\boldsymbol{K}$ denote the relative and c.m. momenta of two nucleons below ε_F. The factor $(k_F^2-K^2-k_0^2)/k_0K$ in the second integral results from integrating over $\cos\theta_{Kk_0}$ with $\cos\theta_{Kk_0} < (k_F^2-K^2-k_0^2)/2Kk_0$ for two particles in the Fermi sea [16]).

Following the same procedure as in the single-particle spectrum case, we simplify (3.21) by the approximation $G^{\alpha}_{LL}(K; k_0, k_0) \equiv G^{\alpha}_{LL}(\tilde{K}_{av}; k_0, k_0)$. Here $\tilde{K}_{av}$ refers to the average value of K for two particles below the Fermi sea with relative momentum k_0; this average c.m. momentum is given by [12])

$$\tilde{K}_{av}^2 = \tfrac{3}{5}k_F^2\left(1-\frac{k_0}{k_F}\right)\left[1+\frac{k_0^2/k_F^2}{3(2+k_0/k_F)}\right]. \quad (3.22)$$

The above expression for $\tilde{K}_{av}$ should not be confused with the definition of K_{av} in the single-particle spectrum case. That determination of K_{av} (3.19) involved the additional constraint of fixing k_μ.

In the average c.m. momentum approximation, the expression for the ground state energy per particle is simply

$$\frac{E}{A} = \tfrac{3}{5}\varepsilon_F + \frac{4}{\pi}\frac{\hbar^2}{M}\sum_{(\alpha L)}(2J+1)(2T+1)\int_0^{k_F} k_0^2\, dk_0\left(1-\frac{3}{2}\frac{k_0}{k_F}+\frac{1}{2}\frac{k_0^3}{k_F^3}\right) G^{\alpha}_{LL}(\tilde{K}_{av}; k_0, k_0). \quad (3.23)$$

The ground state energy of nuclear matter, according to (3.23), consists of the kinetic energy plus a summation of potential energy contributions from each of the allowed eigenstates of the two-body system.

The numerical integration of (3.23) is done by a ten-interval Simpson's rule. Doubling the intervals to 20 changes the numerical evaluation of the total nuclear binding energy by an insignificant amount (< 0.001 MeV).

Table 3 gives the binding energy of nuclear matter determined using 10, 15 and 25 Laguerre-point matrix inversion to calculate G. These values are also compared to the binding energy determined using the analytic G matrix elements (3.16). The potential employed for the test results in table 3 is the extremely strong separable potential mentioned previously. The matrix inversion result using 10 Laguerre points comes to within 2 % of the analytic result. For 25 Laguerre-point matrix inversion,

TABLE 3

The $^1S_0$ potential energy per particle obtained by matrix inversion calculation of the G-matrix

Laguerre points	Potential energy per particle (MeV)
$N = 10$	−91.86
$N = 15$	−88.04
$N = 25$	−89.52
analytic	−89.98

The analytic result (3.16) is also shown. The strong separable potential was used. All calculations are for $k_F = 1.45$ fm^{-1}, $M^*/M = 0.8$ and $U_0 = 80$ MeV.

the discrepancy is only 0.5 %. For realistic potentials even better precision is obtained. The improvement in precision as one increases the number of integration points from 10 to 25 shows that the binding energy calculated by matrix inversion converges to the analytic value for a sufficient number of integration points.

As a further check on the matrix inversion method, we calculated the binding energy of nuclear matter for the Reid Yukawa-core potential [1]) and compare our results to those obtained by Sprung [12]), and by Kallio and Day [12]) in table 4. A more

TABLE 4

State by state comparison of the potential energies per nucleon obtained by matrix inversion with those obtained by Sprung, and by Kallio and Day

	Potential energy per particle (MeV/A)		
state	$N = 16$	Sprung	Kallio and Day
$^1S_0$	−15.57	−15.42	−15.52
$^1D_2$	− 2.55	− 2.54	− 2.56
$^1P_1$	2.39	2.40	2.38
$^3S_1$	−15.16	−14.50	−14.99
$^3D_1$	1.45	1.46	1.46
$^3D_2$	− 4.32	− 4.30	− 4.33
$^3P_0$	3.32	− 3.30	− 3.31
$^3P_1$	9.92	9.90	9.92
$^3P_2$	− 7.05	− 7.03	− 7.06
M^*/M	.64		.60
U_0	79.05		81.00

The potential is the Reid Yukawa-core [ref. [1])]. Self-consistent values of M^* and U_0 and higher partial waves are included in the matrix inversion calculation. In all cases $k_F = 1.36$ fm^{-1}. A Gaussian integration routine is used.

detailed calculation for the Reid potential appears in sect. 5, but some partial results are presented now for comparison. The binding energies given in table 4 are for $k_F = 1.36$ fm^{-1} with the self-consistent M^* and U_0 (sect. 5). The matrix-inversion binding energies agree extremely well with the binding energies obtained by Sprung,

and by Kallio and Day, except for the $^3S_1$ state [12]). Our calculations gave 0.6 MeV more binding in the $^3S_1$ state than the calculation of Sprung, and 0.2 MeV more binding than the calculation of Kallio and Day. Kallio and Day state that the disagreement between their binding energies and those of Sprung is probably due to the neglect of higher-order terms in Sprung's reference-spectrum calculation. In our calculation the quantities M^* and U_0 were calculated self-consistently and higher partial waves were included. After adjustment of the Kallio-Day values to include the self-consistent M^* and U_0, one finds excellent agreement to within 0.03 MeV/A [ref. [17])].

This excellent agreement with published values is not surprising since similar methods are used except for the evaluation of G by matrix inversion. Therefore, table 4 is strong evidence for the reliability of matrix inversion in calculating G-matrices. Of course, its full advantage appears mainly for nonlocal potentials.

4. Smooth triplet-even potentials

With the techniques developed in the last two sections, we can handle the two-body scattering and nuclear matter problems for general non-local potentials. Our first application is to develop smooth nonlocal potentials that are adjusted to fit the triplet-even eigenphase shifts. Later these potentials will be part of our study of various potentials in nuclear matter.

The idea of using smooth potentials originated with Peierls, Green and Levinger [18]). They showed that the two-nucleon data could be matched using a velocity-dependent potential instead of a hard-core repulsion. However, these potentials were not smooth enough to be used in a rapidly convergent perturbation theory of nuclear structure. Examples of smoother nonlocal, or velocity-dependent, potentials were suggested later [2,19]). The extra smoothness was generated by phenomenological reduction of the off-energy-shell R-matrix elements. Extensive and impressive use has been made of these smooth potentials in nuclear structure calculations [20]); the search for improved smooth potentials continues [21]). In this section an attempt is made to extend the idea of smoothness, by reduction of off-energy-shell matrix elements, to the tensor force.

Use of standard local tensor interactions requires one to include higher order terms in perturbative calculations. It was our hope originally that a nonlocal tensor force could be developed that would fit the eigenphases, provide saturation of nuclear matter, and yet be weak enough to permit first order perturbative calculations in nuclear structure studies. Here we present two examples of weak tensor forces that do indeed yield fits to the eigenphases and for which ordinary perturbation theory has an amazingly rapid convergence rate. Unfortunately, they yield convergence to the wrong answer for the binding energy (sect. 5). Thus we are forced to consider these forces unrealistic if one requires, as we do, that proper saturation be found. Nevertheless, it is very instructive to consider these examples of smooth interactions, as is discussed in sect. 5.

For a given spin and isospin, consider the nucleon-nucleon potential to be a function of the relative coordinates $\boldsymbol{r}$, relative momentum $\boldsymbol{p}$, and the spins

$$V^{ST}(\boldsymbol{r}, \boldsymbol{p}, \boldsymbol{\sigma}_1, \boldsymbol{\sigma}_2) = V_A + \tilde{V}_R + V_{s.o.} + V_T + \tilde{V}_{TA} + \tilde{V}_{TB}. \tag{4.1}$$

The nonlocal terms are marked by the tilde. Here V_A is a local, central attraction, which is assumed to be of Gaussian form

$$V_A \equiv V_A(r) = V_A' e^{-(a_A r)^2}. \tag{4.2}$$

The nonlocal repulsion $\tilde{V}_R$ is given by

$$\tilde{V}_R = \tfrac{1}{2}[C_R(p^2)V_R(r) + V_R(r)C_R(p^2)], \tag{4.3}$$

where $V_R(r)$ is again of Gaussian form and the operator $C_R(p^2)$ is

$$C(p^2) = \left(\frac{p}{\hbar a}\right)^2 e^{-(sp/\hbar)^2}. \tag{4.4}$$

This exponential velocity dependence is a extension of the quadratic case ($s = 0$) introduced by Peierls, Levinger and Green [18]). In momentum space the matrix elements are very simple

$$\langle k|\tilde{V}_R|k'\rangle = \tfrac{1}{2}[C_R(k^2) + C_R(k'^2)]\langle k|V_R|k'\rangle. \tag{4.5}$$

Here it is seen that $C(k^2)$ acts as a cut-off in momentum space; the higher momentum components are thereby removed and $\tilde{V}_R$ corresponds to a smooth repulsion. Thus we refer to s as the smoothness parameter.

The spin-orbit interaction is taken to be different for each value of the total angular momentum J. We use $V_{s.o.} = V_{s.o.}^{(J)}(r)(\boldsymbol{L}\cdot\boldsymbol{S})$ with $V_{s.o.}^{(J)}$ taken as a sum of Gaussians, $V_{s.o.1}^{(J)} \exp(-a_{s.o.1}r^2) + V_{s.o.2}^{(J)} \exp(-a_{s.o.2}^2 r^2)$. The extra parameters are needed to produce a fit to both $^3D_1$ and $^3D_2$ phase shifts. For $J = 1$, we have set $V_{s.o.2}^{(1)} = 0$, but $V_{s.o.2} \neq 0$ is needed for the $^3D_2$ phase shift. This dependence on the J-value simulates the effect of a quadratic spin-orbit $(\boldsymbol{L}\cdot\boldsymbol{S})^2$ term.

The local tensor term is $V_T = V_T(r)S_{12}(\hat{r})$, with $V_T(r)$ chosen for convenience to be of the form $(ar)^2 e^{-(ar)^2}$. This form enables us to find simple analytic expressions for the momentum space matrix elements [ref. [16])]. The tensor operator $S_{12}(r) = 3(\boldsymbol{\sigma}_1\cdot\hat{r})(\boldsymbol{\sigma}_2\cdot\hat{r}) - \boldsymbol{\sigma}_1\cdot\boldsymbol{\sigma}_2$ is the standard one.

The additional tensor terms are $\tilde{V}_{TA}$ and $\tilde{V}_{TB}$. These terms involve the momentum cut-off operator $C(p^2)$ and are defined by

$$\tilde{V}_{TA} = \tfrac{1}{2}[V_{TA}(r)S_{12}(\hat{p})C_A(p^2) + C_A(p^2)S_{12}(\hat{p})V_{TA}(r)], \tag{4.6}$$

$$\tilde{V}_{TB} = \tfrac{1}{2}[V_{TB}(r)S_{12}(\hat{r})C_B(p^2) + C_B(p^2)S_{12}(\hat{r})V_{TB}(r)]. \tag{4.7}$$

Here $S_{12}(\hat{p})$ is the velocity dependent or nonlocal tensor operator $S_{12}(\hat{p}) = 3(\boldsymbol{\sigma}_1\cdot\hat{p})(\boldsymbol{\sigma}_2\cdot\hat{p}) - \boldsymbol{\sigma}_1\cdot\boldsymbol{\sigma}_2$. The same cut-off forms, $C(p^2)$, are used, but with independent smoothness parameters s_A and s_B. When used in (4.1) we refer to $\tilde{V}_{TA}$ and $\tilde{V}_{TB}$

as potentials A and B, respectively. The form $(ar)^2 e^{-(ar)^2}$ is again used for $V_{TA}(r)$ and $V_{TB}(r)$.

Nonstatic tensor operators such as $(\boldsymbol{\sigma}_1 \cdot \boldsymbol{p})(\boldsymbol{\sigma}_2 \cdot \boldsymbol{p})$ have been discussed by Okubo and Marshak [22]). They show that these operators are equivalent to the local tensor operator $(\boldsymbol{\sigma}_1 \cdot \boldsymbol{r})(\boldsymbol{\sigma}_1 \cdot \boldsymbol{r})$ for the S-matrix or the on-energy-shell scattering amplitude. However, we are concerned not only with the scattering amplitude, but also with the off-energy-shell matrix elements of the tensor potential. In fact, the tensor interactions are not equivalent to each other, but have distinctly different off-energy-shell matrix elements.

For the nonlocal tensor terms (4.6 and 4.7) these matrix elements in the eigenchannel $\alpha LL'$ are of the form [16])

$$\tilde{v}^{\alpha}_{LL'}(k|k') = i^{L-L'} A^{JS}_{LL'} \tfrac{1}{2}[C_A(k'^2) v^{\alpha}_{LL}(k|k') + C(k^2) v^{\alpha}_{L'L'}(k|k')], \tag{4.8}$$

for $\tilde{V}_{TA}$ and

$$\tilde{v}^{\alpha}_{LL'}(k|k') = A^{JS}_{LL'} \tfrac{1}{2}[C_B(k^2) + C_B(k'^2)] v^{\alpha}_{LL'}(k|k'), \tag{4.9}$$

for $\tilde{V}_{TB}$. Here $A^{JS}_{LL'} \equiv \langle JMLS|S_{12}|JMLS\rangle$. The matrix element $V^{\alpha}_{LL'}(k|k')$ is obtained from the local functions $V_{TA}(r)$ or $V_{TB}(r)$; for example,

$$v^{\alpha}_{LL'}(kk') = \int_0^{\infty} j_L(kr) r^2 \, dr V_{TB}(r) j_{L'}(k'r). \tag{4.10}$$

The matrix elements for a local tensor potential can be obtained from (4.9) by setting $C_B(k^2)$ equal to unity. It is clear from (4.8 and 4.9) that nonlocal tensor potentials are not equivalent to the local tensor potential. Indeed, very different matrix elements are produced by nonlocal tensor interactions.

The main characteristic that is changed by introduction of nonlocal tensor potentials is the matrix element $V^{\alpha}_{J-1,J+1}(k|k')$. For example, in the ${}^3S_1 + {}^3D_1$ coupled state the S–D matrix element $V_{02}(k|k')$ has a peak when considered as a function of k' for fixed k. The location and height of that peak depends on the strength and range of the tensor term; for the Reid potential a peak occurs at about $k' \approx 2$ fm^{-1}. A nonlocal tensor potential can alter the peak in $V_{02}(k|k')$ considerably. Nonlocal tensor potentials should therefore cause significant changes in the two-body wave functions, both for free scattering and in the nuclear medium (see eq. 5.2). These characteristics will be discussed later (sect. 5).

The most difficult part of the parameter search is to fit the mixing parameter $\varepsilon_1(k)$, while keeping the potential as smooth as possible. The usual claim is that the $\varepsilon_1(k)$ curve, along with the properties of the deuteron, require a strong tensor interaction. In our counterexample we generate a weak tensor potential by using nonlocal terms to fit $\varepsilon_1(k)$. A local tensor potential of relatively long range can produce the correct low-energy, but not the high-energy behavior of $\varepsilon_1(k)$ (see fig. 3). One way of handling that situation is to decrease the tensor force range and/or by introducing a strong short-range tensor repulsion. Those procedures yield a strong tensor potential.

Alternately, one can use a nonlocal tensor force, which is adjusted to dominate at higher energies (fig. 3). In combination with a local tensor term, a nonlocal tensor potential can produce a fit to the $\varepsilon_1(k)$ curve as illustrated in fig. 3. However, in this

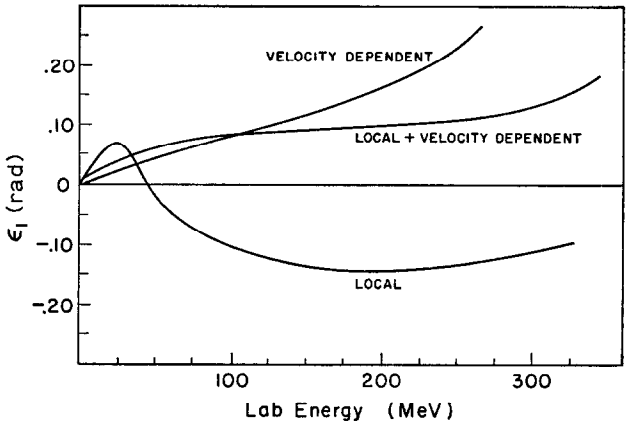

Fig. 3. The mixing parameter $\varepsilon_1(k)$ for a long-range local tensor force and for a velocity-dependent tensor force. A combination of a weak local and weak nonlocal tensor can produce agreement with the experimental $\varepsilon_1(k)$.

case both the local and nonlocal terms are relatively weak. The fact that weak tensor forces are indeed produced by this procedure is demonstrated clearly in sect. 5 (see fig. 8).

TABLE 5

Parameters for potentials A and B

Potential	(MeV)							
	v_A	v_R	$v_{s.o.1}^{(1)}$	$v_{s.o.1}^{(2)}$	$v_{s.o.2}^{(2)}$	v_T	v_{TB}	v_{TA}
A	−186.0	7200.0	−423.0	28.0		5.55		1005.0
B	− 97.6	7200.0	− 6.3	5.0	−1400.0	−25.0	−840.0	
	$(\text{fm})^{-1}$							
	a_A	a_R	$a_{s.o.1}^{(1)}$	$a_{s.o.1}^{(2)}$	$a_{s.o.2}^{(2)}$	a_T	a_{TB}	a_{TA}
A	1.00	2.80	1.10	0.53	1.60	0.44		2.20
B	0.79	2.80	0.40	0.34		0.73	1.80	
	$(\text{fm})^{-1}$							
		s_p		s_{TB}		s_{TA}		
A		0.530				0.785		
B		0.544		0.640				

The potential strengths, ranges, and smoothness parameters were adjusted to produce a fit to the Yale (Y–IV) phase shifts [23]) transformed to the Blatt-Biedenharn convention. These parameters are given in table 5, the resulting fits are shown in

TABLE 6
Effective range and deuteron data for potentials A and B

	A	B	Experiment
a_T (fm)	5.404	5.391	5.392±0.006
r_{0T} (fm)	1.738	1.731	1.726±0.014
E_B (MeV)	2.28	2.28	2.22
Q (fm^2)	0.254	≈0.12	0.278
P_D(%)	2.00	2.01	4–8

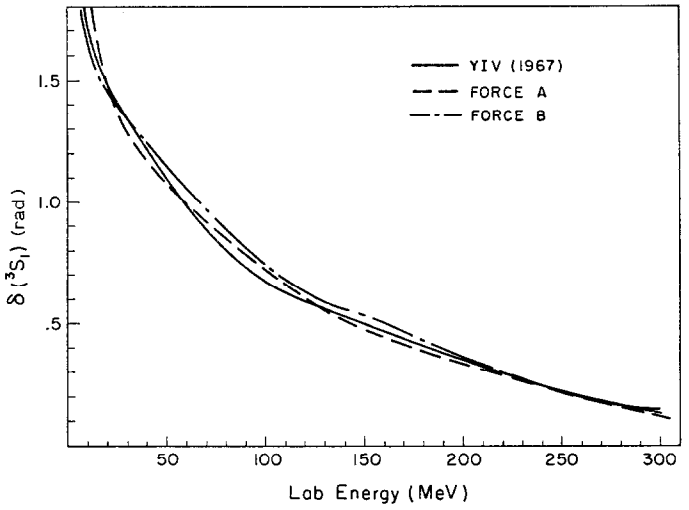

Fig. 4. The $^3S_1$ eigenphase shift for potentials A and B compared to Y–IV [ref. [23])].

figs. 4–6. Direct matrix inversion with 15 Laguerre points sufficed to yield accurate phase shifts. The effective range, scattering length, binding energy, and D-state probability for the $^3S_1+{}^3D_1$ state are given in table 6. The electric quadrupole moments were first estimated using $\varepsilon_1(k) \approx \sqrt{2}\, Qk^2$ and were later calculated precisely[28]). The electric quadrupole could probably be fitted accurately without major changes in the potential. However, the low D-state probability is most likely an inescapable result of using weak tensor interactions. The fit to ε_1 is not perfect, but there are large experimental uncertainties in ε_1 [ref. [23])].

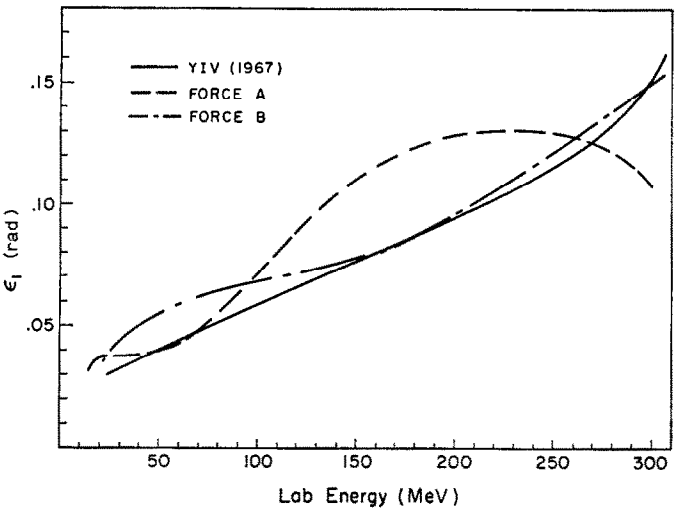

Fig. 5. The mixing parameter $\varepsilon_1(k)$ for potentials A and B compared to Y–IV [ref. [23])].

The phase-shift fits in figs. 4–6 are sufficiently precise for our present study of nuclear matter binding energies. To carry out that study, our triplet-even example is supplemented by the triplet-odd, singlet-even, and singlet-odd interactions of ref. [2]).

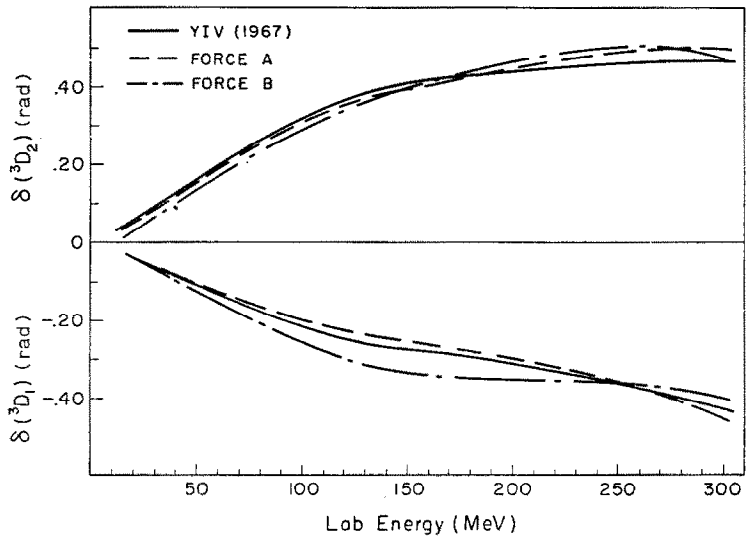

Fig. 6. The $^3D_1$ and $^3D_2$ phase shifts for potentials A and B compared to Y–IV [ref. [23])].

5. Saturation and smoothness

Smooth potentials with weak tensor interactions can be devised to fit the two-nucleon data, (sect. 4). Now we use those smooth potentials, along with stronger ones, to ask a general question. How does the saturation of nuclear energy and density depend upon the smoothness of the two-nucleon potential?

Our approach to this problem is to do a series of nuclear matter calculations with potentials of varying smoothness. A quantitative measure of smoothness is provided in the following discussion. Later, we will deal with five different potentials and consider the resulting saturation properties. A clear relationship between saturation and smoothness then emerges.

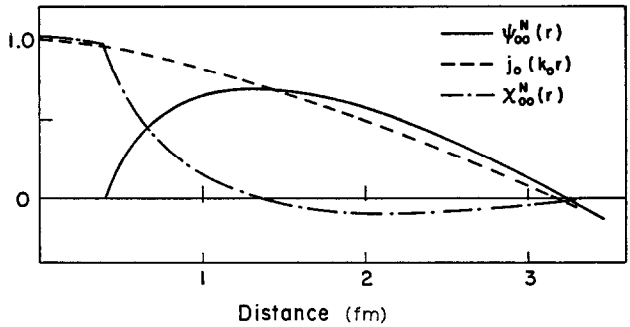

Fig. 7. The Bethe-Goldstone relative wave function ψ^N_{00} (eq. 5.2.), for $^1S_0$ state. The unperturbed wave function is $j_0(k_0 r)$ and the wave function defect is $\chi_{00}(r)$. This case is for a hard-core of 0.4 fm range plus an attractive tail. The value $k_F = 1.5$ fm^{-1} and $k_0 = 0.9$ fm^{-1} were used.

5.1. SMOOTHNESS

To provide a quantitative measure of the smoothness of a given two-nucleon, let us consider the wave function defect defined by

$$\xi_{\mu\nu}(\boldsymbol{r}) = (2\pi)^{\frac{3}{2}}[\phi_{\mu\nu}(\boldsymbol{r}) - \psi^N_{\mu\nu}(\boldsymbol{r})]. \tag{5.1}$$

Here $\phi_{\mu\nu}(r)$ is the unperturbed relative wave function for two nucleons in the orbitals μ and ν, i.e. $\phi_\mu(\boldsymbol{r}_1)\phi_\nu(\boldsymbol{r}_2) = \phi_{\mu\nu}(\boldsymbol{R})\phi_{\mu\nu}(\boldsymbol{r})$. The Bethe-Goldstone wave function $\psi_{\mu\nu}(\boldsymbol{r})$ describes the relative motion of the two nucleons in the Fermi sea. It is determined by

$$\psi^N_{\mu\nu}(\boldsymbol{r}) = \phi_{\mu\nu}(\boldsymbol{r}) - \int \frac{d\boldsymbol{k}\bar{Q}(k', K)G(K|\boldsymbol{k}', \boldsymbol{k}_0)}{E(k', K) - E(k_0, K)} \frac{e^{i\boldsymbol{k}'\cdot\boldsymbol{r}}}{(2\pi)^{\frac{3}{2}}}, \tag{5.2}$$

which follows from (3.12) and the relation $G\phi = V\psi^N$. We use k_0 as the relative momentum $k_{\mu\nu}$.

The important property of the Bethe-Goldstone wave function is that it heals to the unperturbed wave function, $\psi^N_{\mu\nu}(r) \underset{r\to\infty}{\longrightarrow} \phi_{\mu\nu}(r)$. The absence of a phase shift in ψ^N is a direct result of the lack of an energy conserving singularity in (5.2). This healing

property explains the long mean free path of nucleons in nuclei and forms the theoretical basis of the independent particle model of nuclear structure [7, 11]).

At short distances, the Bethe-Goldstone wave function deviates considerably from the unperturbed wave function. The healing property and deviation at short distances are illustrated in fig. 7. It is seen that the wave function defect $\xi_{\mu\nu}(r)$ records these short-range deviations and hence is a measure of the smoothness of the two-nucleon potential. For example, a larger $\xi_{\mu\nu}(r)$ is produced by a stronger potential.

It is more convenient, however, to introduce a number to serve as a measure of smoothness. Correspondingly, we introduce the wound integral κ defined as

$$\kappa = \rho\langle\xi_{\mu\nu}|\xi_{\mu\nu}-\xi_{\nu\mu}\rangle_{\mathrm{av}}, \tag{5.3}$$

where the values of k_{F}, K, and $k_{\mu\nu}(\equiv k_0)$ used are given in table 7. The wound integral is an overall measure of the potential's strength and, correspondingly, of the off-energy-shell matrix elements that determine the short range wave function.

In addition, κ is the important smallness, or expansion parameter, for the nuclear many-body problem. It is also directly related to the ω-dependence of $G(\omega)$, i.e. $\kappa \approx -\rho(\partial/\partial\omega)G(\omega)$. The significance of κ has been discussed extensively by Brandow [7]). For our present discussion, it simply serves as a measure of smoothness.

The wave function defect, $\xi_{\mu\nu}$, can be decomposed into partial waves

$$\xi_{\mu\nu}(r) = \frac{2}{\pi}\sum_{JMLL'} i^L \chi^{\alpha}_{LL'}(r) Y^*_{LML}(\hat{k}_0)\langle LSM_L M_S|JM\rangle \mathscr{Y}^{JM}_{L'S}(\hat{r})|TT_3\rangle. \tag{5.4}$$

Correspondingly, the wound integral can be expressed as a sum of partial wave contributions $\kappa = \sum_{\alpha LL'}\kappa^{\alpha}_{LL'}$, where $\kappa^{\alpha}_{LL'}$ is given by

$$\begin{aligned}\kappa^{\alpha}_{LL'} &= \tfrac{1}{2}\pi\rho(2J+1)(2T+1)\int_0^\infty \mathrm{d}r r^2|\chi^{\alpha}_{LL'}(r)|^2 \\ &= \frac{2}{3\pi^2}k_{\mathrm{F}}^3(2J+1)(2T+1)\int_0^\infty \frac{\mathrm{d}k' k'^2 \bar{Q}^2(k', K)|G^{\alpha}_{L'L}(K|k', k_0)|^2}{|E_<(k', K)-E_<(k_0, K)|^2}.\end{aligned} \tag{5.5}$$

Again average values of k_{F}, K and $k_{\mu\nu}(\equiv k_0)$ are used in evaluating κ. The wound integral $\kappa^{\alpha}_{LL'}$ in a coupled channel consists of four numbers $\kappa^{\alpha}_{J\pm1,J-1}$ and $\kappa^{\alpha}_{J\pm1,J+1}$. For the $^3\mathrm{S}_1+{}^3\mathrm{D}_1$ the wound integrals κ_{00} and κ_{02} are appreciable in magnitude, whereas κ_{22} and κ_{20} are small (see later). The two numbers κ_{00} and κ_{02} therefore measure the smoothness of the central and tensor potentials in the $^3\mathrm{S}_1+{}^3\mathrm{D}_1$ eigen-channel. For the $^1\mathrm{S}_0$ case only one number κ_{00} enters, which measures the smoothness of the $^1\mathrm{S}_0$ central potential. These quantities are calculated for each potential and later are seen to play a crucial role in saturation.

A more detailed picture of the wave function defect can be obtained by considering the Bessel transform

$$F^{\alpha}_{LL'}(k) \equiv k\int_0^\infty \mathrm{d}r r^2 j_{L'}(kr)X^{\alpha}_{LL'}(r) = \frac{k\bar{Q}(k, K)G_{L'L}(K|k, k_0)}{E_<(k_0 K)-E_>(k, K)}. \tag{5.6}$$

Formally, $F^{\alpha}_{LL'}$ is defined by $\phi - \psi = F = (Q/e)G$ or equivalently $V - G = VF$. The quantity $F^{\alpha}_{LL'}$ (k) is the probability amplitude for exciting two nucleons of relative orbital angular momentum L, relative momentum k_0, to a state with relative angular momentum L' and relative momentum k. The c.m. momentum stays unchanged. Thus $F^{\alpha}_{LL'}(k)$ tells us which intermediate states enter significantly into the determination of ψ^{N} and of the G-matrix. Its full significance will be seen later.

Both $\kappa^{\alpha}_{LL'}$ and $F^{\alpha}_{LL'}$ are useful measures of smoothness. Stronger potentials increase both quantities. In fact, they are not independent, but are related by

$$\kappa^{\alpha}_{LL'} = \frac{2}{3\pi^2} k_F^3 (2T+1)(2J+1) \int_0^{\infty} dk' |F^{\alpha}_{LL'}(k')|^2. \tag{5.7}$$

Together κ and F provide a picture of the wave function defect and are a direct measure of the strength or smoothness of a given two-nucleon potential. They can be obtained from (5.6) and (5.7) once the G-matrix is known.

5.2. DESCRIPTION OF THE CALCULATIONS

The nuclear matter calculations involve solving for the G-matrix by the matrix inversion method previously described (sect. 3). The angle-averaged Pauli operator, the effective mass spectrum, and the average c.m. approximations described in sect. 3 are made for all cases. Sixteen Gaussian points are used in the matrix inversion for all cases except potentials A and B (sect. 4). For potentials A and B fifteen Laguerre points suffice to solve for the G-matrix. The finite integrals for the single-particle potential (3.20) and total binding energy (3.23) are evaluated using a ten-point Simpson's rule. The single-particle spectrum is always treated self-consistently; the self-consistent values of M^* and U_0 are quoted later.

Once the G-matrix and self-consistent spectrum are determined, the quantities $\kappa^{\alpha}_{LL'}$ and $F^{\alpha}_{LL'}$ are obtained from (5.6) and (5.7). The integral involved in (5.7) is also done numerically.

This procedure is repeated for each potential and the matrix elements $v^{\alpha}_{LL'}(k|k')$ are needed for each case. For the Reid [1]) and Bryan-Scott [5]) potentials the matrix elements are obtained using the steps outlined in the appendix. The Bryan-Scott case is a nonlocal potential having quadratic velocity dependence. The Appel [6]) potential has Yukawa form plus a nonlocal tensor potential similar to those described in sect. 4. The momentum space matrix elements of potentials A and B were presented in sect. 4. All of these potentials, both local and nonlocal, are easily handled in momentum space (appendix). The contribution of higher partial waves, up to $L = 7$, are included in our nuclear matter calculations. For the Reid case, the one-pion-exchange term (OPEP), including a cut-off of its r^{-3} singularity, is used for all states not explicitly fitted by Reid. It is found that $G \approx V$ is a good approximation for higher ($J \geqq 3$) partial waves, except for the coupled ${}^3D_3 + {}^3G_3$ state for which the full G-matrix is needed. The phase-shift approximation is not employed, but would be a better

procedure for ($J \geqq 3$) states having phase shifts that are known to deviate from the OPEP values [24]).

For potentials A and B the higher partial waves ($J \geqq 3$) were taken from the Reid case. The complete Bryan-Scott potential was used to calculate the contribution of its higher partial waves to the binding energy; the approximation $G \approx V$ was again used, when applicable.

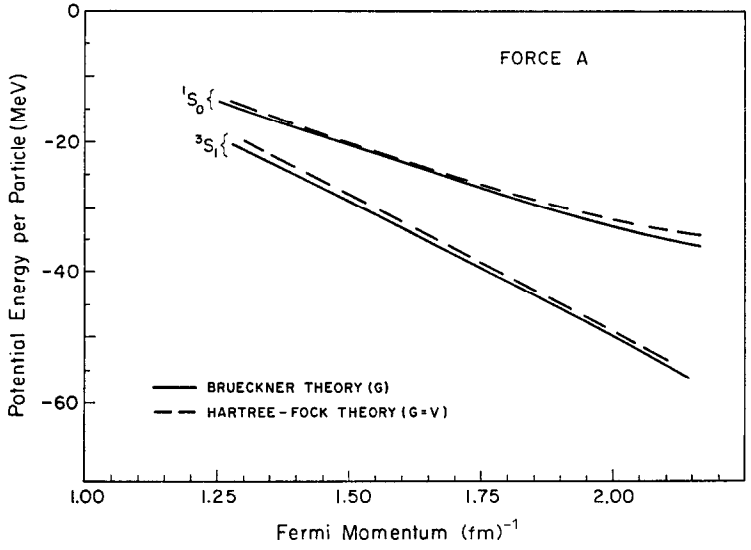

Fig. 8. The S-wave potential energy per nucleon for potential A computed using the Brueckner (G) and Hartree-Fock (G ≈ V) approximations.

For the Appel potential higher partial waves were not included. Only the singlet and triplet-even parts of the Appel potential are used here since Appel's potential gives a poor P-wave fit. Therefore, we follow the suggestion of Bhargava and Sprung [24]) and include just the $^1S_0$, $^1D_2$ and $^3S_1 + ^3D_1$ states for the Appel case. These approximations suffice for our study of the relation between saturation and smoothness. The Appel potential is of interest since it has a nonlocal tensor term of intermediate smoothness.

5.3. CLASSIFICATION OF THE POTENTIALS

Potentials A and B of sect. 4 provide examples of smooth nonlocal potentials that fit the $^3S_1 + ^3D_1$ eigenphases. Their extreme smoothness is demonstrated by figs. 8 and 9. Here the $^3S_1$ and $^1S_0$ potential energies per particle are compared for the full G-matrix case (Brueckner theory) and for the first-order perturbation or Hartree-Fock approximation of $G \approx V$. First order perturbation theory works very well since the sum of higher order terms, $V + V(Q/e)V + \ldots$, is only 1 MeV/A and 4 MeV/A for

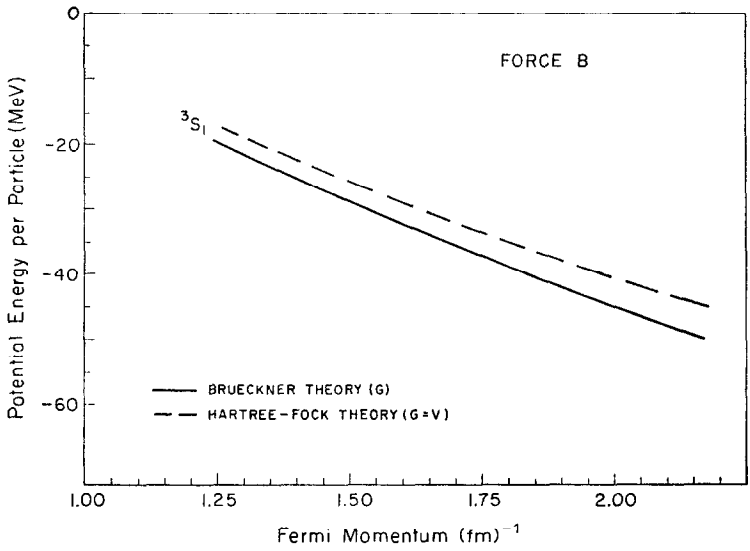

Fig. 9. The $^3S_1$ potential energy per nucleon for potential B computed using the Brueckner (G) and Hartree-Fock (G $\approx$ V) approximations.

potentials A and B, respectively (figs. 8, 9). This should be compared to the Reid case, where these higher order terms are essential (fig. 10). Figs. 8–9 also show that potential B is somewhat stronger than potential A.

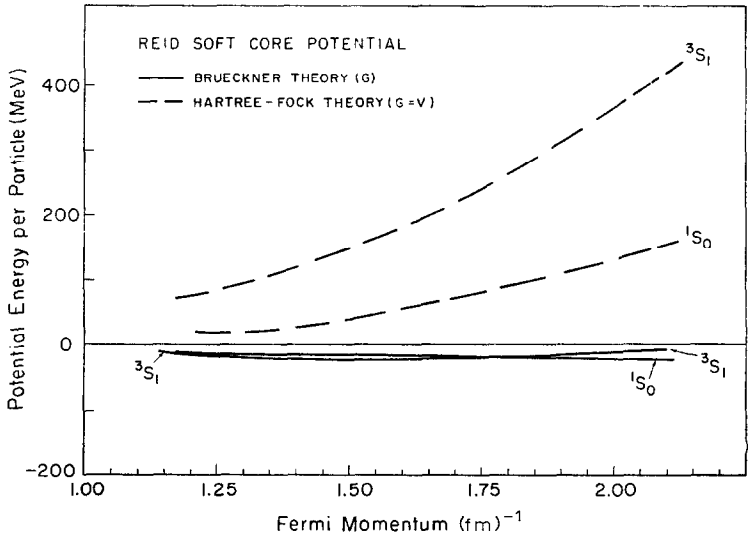

Fig. 10. The S-wave potential energy per nucleon for the Reid Yukawa-core potential computed using the Brueckner (G) and Hartree-Fock (G $\approx$ V) approximations. Note the large energy scale.

Although excellent convergence of ordinary perturbation theory is obtained for potentials A and B, they unfortunately do not produce proper saturation. This failure to produce the correct saturation property is not due to their phase-shift fit, but appears to be a direct consequence of their extreme smoothness.

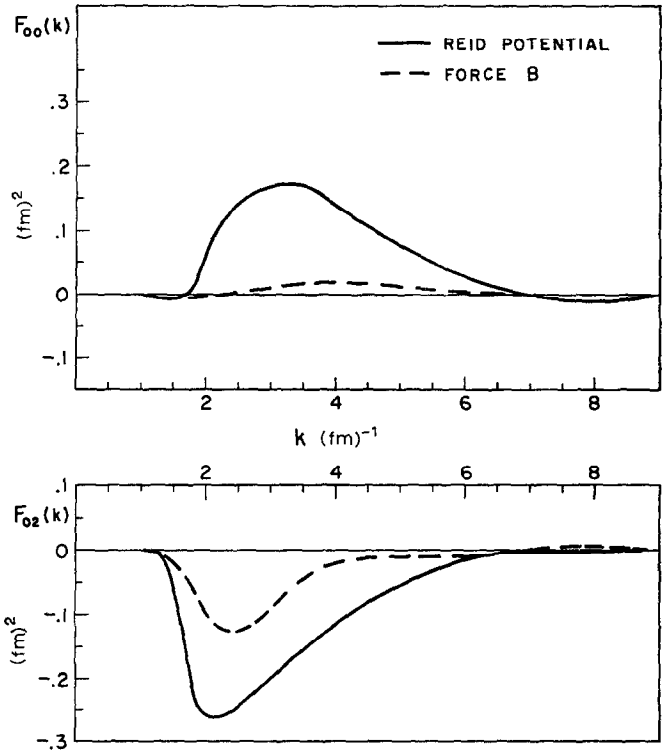

Fig. 11. The Bessel transforms of the wave function defect for the $^3S_1+^3D_1$ eigenchannel, $F^{\alpha}_{00}(k)$ and $F^{\alpha}_{02}(k)$. The results for the Reid and for potential B are shown. Here $k_0 = 0.9$ fm^{-1}, $k_F = 1.5$ fm^{-1}, and $K = \bar{K}_{av}$ as defined by eq. (3.22) were used.

To understand the relationship between smoothness and saturation, we must classify the various potentials as to their smoothness. The wound integral κ, and Bessel transform of the wave function defect provide us with the needed measure of smoothness. In table 7 the values of $\kappa^{\alpha}_{LL'}$ are given for each of the potentials considered. The values of k_0, K_{av} and k_F are also stipulated. The values given in table 7 result from a self-consistent calculation of the G-matrix including higher partial waves. It is clear from table 7 that κ_{00} for $^1S_0$ and κ_{00}, κ_{02} for $^3S_1+^3D_1$ are the dominant terms of κ.

The value of $\kappa^{\alpha}_{LL'}$ and κ given in table 7 for the Reid potential are in excellent agreement with other published results [12]). That agreement is strong evidence for the reliability of the matrix inversion method used here.

The potentials are ordered in table 7 according to decreasing κ or increasing

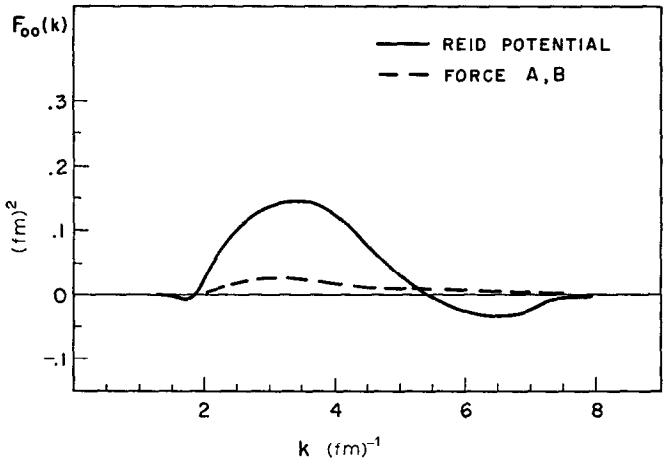

Fig. 12. The Bessel transform of the wave function defect for the $^1S_0$ state, $F^{\alpha}_{00}(k)$. The results for the Reid and for potentials A, B are shown. Here $k_0 = 0.9$ fm^{-1}, $k_F = 1.5$ fm^{-1}, and $K = \bar{K}_{av}$ as defined by eq. (3.22) were used.

smoothness. It is seen that κ ranges from 0.1589 for the strong Reid potential to 0.0137 for the smoothest case-potential A. This decrease of κ arises from the corresponding decrease in $\kappa^{\alpha}_{LL'}$. The value of $\kappa_{00}(^1S_0)$ decreases from 0.0284 all the way

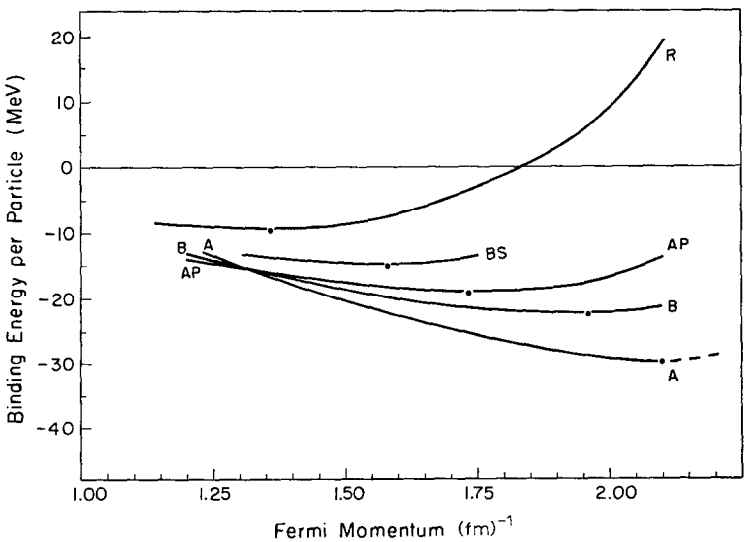

Fig. 13. The total binding energy per nucleon as a function of density as measured by k_F, the Fermi momentum. Abbreviations used are: R-Reid, BS-Bryan-Scott, AP-Appel, B-potential B, and A-potential A. Increased binding and increased density are seen to be correlated with increased smoothness (table 7).

down to 0.0006. Similarly, for the $^3S_1+{}^3D_1$ coupled state the variation in κ_{00} is from 0.0385 to 0.0022 and in κ_{02} from 0.0711 to 0.0004.

The Bessel transforms of the wave function defect $F^a_{LL'}(k)$ are shown in figs. 11 and 12 for the Reid potential and for potentials A and B. The other potentials yield intermediate values of $F^a_{LL'}(k)$. The important properties of $F^a_{LL'}(k)$ are the peaks in $F_{00}(k)$ at $k \approx 3\ \mathrm{fm}^{-1}$ and in $F_{02}(k)$ at $k \approx 2\ \mathrm{fm}^{-1}$. For smooth potentials these peaks occur at about the same values of k, but with greatly reduced height. That means smooth potentials are less likely to excite two nucleons to a value of k near 2 or 3 fm^{-1}. As the density of nuclear matter is increased, the Pauli operator projects out states of increasing relative momentum. Consequently, the reduced peaks shown in figs. 11 and 12 are expected to change the potential energy versus density curves. The question is: how much of a change is produced by the reduced peaks in $F^a_{LL'}(k)$? Also, are the changes in the $^1S_0$ case or the $^3S_1$ case more crucial?

5.4. THE SATURATION CURVES

The binding energy per nucleon as a function of the Fermi momentum, k_F, is given in fig. 13 for five potentials. A definite pattern is seen. The smoother potentials give more binding and a larger equilibrium density. This pattern follows exactly the order provided by the values of κ given in table 7. The smoothest case, potential A, produces saturation but with an overbinding of -15 MeV and at too large a Fermi momentum, $k_F \geqq 2.1\ \mathrm{fm}^{-1}$. The somewhat stronger case, potential B, gives less binding and a lower k_F, but it is still far from producing correct saturation.

TABLE 7

Wound integrals κ for potentials studied

	Reid [a]) ($k_0 = 0.9$, $k_F = 1.5$)	Bryan-Scott ($k_0 = 0.912$, $k_F = 1.52$)	Appel ($k_0 = 0.9$, $k_F = 1.5$)	Force B ($k_0 = 0.9$, $k_F = 1.5$)	Force A ($k_0 = 0.9$, $k_F = 1.5$)
$^1S_0$	0.0284	0.0157	0.0082	0.0006	0.0006
$^1D_2$	0.0002	0.0001	0.0001	0.0003	0.0003
$^1P_1$	0.0051	0.0008		0.0019	0.0019
$^3S_1+{}^3D_1(\kappa_{00})$	0.0385	0.0111	0.0004	0.0008	0.0022
$^3S_1+{}^3D_1(\kappa_{02})$	0.0711	0.0576	0.0241	0.0135	0.0004
$^3D_1$		0.0002	0.0001		0.0004
$^3D_2$	0.0003	0.0005		0.0004	0.0002
$^3P_0$	0.0042	0.0037		0.0006	0.0006
$^3P_1$	0.0058	0.0106		0.0009	0.0009
$^3P_2+{}^3F_2(\kappa_{11})$	0.0033	0.0014		0.0015	0.0015
$^3P_2+{}^3F_2(\kappa_{13})$	0.0030	0.0027		0.0037	0.0037
$^3P_2+{}^3F_2(\kappa_{31})$					
$^3F_2$					
total κ	0.1589	0.1044	0.0329	0.0242	0.0137

The $K_{\alpha\nu}$ defined by (3.22) was used. The values of k_F and of $k_{\mu\nu} \equiv k_0$ used to evaluate κ are shown.
[a]) At $k_F = 1.36\ \mathrm{fm}^{-1}$ our value of κ agrees with the result given in ref. [24]).

TABLE 8

Binding energy of nuclear matter for the Reid Yukawa-core potential

	Potential energy per particle (MeV/A)			
k_F(fm^{-1}) State	1.20	1.36	1.50	1.80
$^1S_0$	−12.25	−15.57	−18.43	−23.97
$^1D_2$	− 1.48	− 2.55	− 3.88	− 8.25
$^1G_4$	− 0.24	− 0.47	− 0.77	− 1.86
$^1I_6$	− 0.05	− 0.11	− 0.19	− 0.54
$^1P_1$	1.29	2.39	3.88	9.36
$^1F_3$	0.48	0.84	1.28	2.67
$^1H_5$	0.10	0.21	0.36	0.91
$^1J_7$	0.02	0.05	0.10	0.32
$^3S_1$	−13.19	−15.16	−16.16	−15.84
$^3D_1$	0.88	1.45	2.11	4.01
$^3D_2$	− 2.58	− 4.32	− 6.36	−12.52
$^3D_3$	0.17	0.32	0.52	1.18
$^3G_3$	0.10	0.21	0.36	0.95
$^3G_4$	− 0.36	− 0.72	− 1.20	− 2.95
$^3G_5$	0.04	0.09	0.16	0.45
$^3I_5$	0.02	0.04	0.07	0.22
$^3I_6$	− 0.07	− 0.16	− 0.30	− 0.87
$^3I_7$	0.01	0.16	0.03	0.12
$^3P_0$	− 2.36	− 3.32	− 4.20	− 5.74
$^3P_1$	6.14	9.93	14.37	28.19
$^3P_2$	− 4.21	− 7.05	−10.41	−20.84
$^3F_2$	− 0.30	− 0.55	− 0.89	− 2.02
$^3F_3$	0.86	1.56	2.43	5.26
$^3F_4$	− 0.10	− 0.21	− 0.36	− 0.93
$^3H_4$	− 0.04	− 0.09	− 0.16	− 0.45
$^3H_5$	0.16	0.33	0.59	1.58
$^3H_6$	− 0.02	− 0.04	− 0.07	− 0.22
$^3J_6$	− 0.01	− 0.02	− 0.03	− 0.11
$^3J_7$	0.03	0.08	0.15	0.49
$^3J_8$	− 0.002	− 0.01	− 0.02	− 0.06
totals				
S	−25.45	−30.74	−34.59	−39.81
P	0.86	1.95	3.65	10.96
D	− 3.01	− 5.10	− 7.60	−15.58
F	0.94	1.63	2.46	4.99
G	− 0.46	− 0.89	− 1.46	− 3.42
H	0.20	0.41	0.72	1.82
I	− 0.10	− 0.21	− 0.39	− 0.97
J	0.05	0.11	0.21	0.64
$J \geqq 3$	1.10	1.92	2.94	6.26
$^3P_0+^3P_1+^3P_2$	− 0.43	− 0.44	− 0.23	1.60
P+D	− 2.15	− 3.15	− 3.95	− 4.62
total potential energy	−26.99	−32.87	−37.09	−41.95
kinetic energy	17.92	23.01	27.99	40.31
total binding energy	− 9.07	− 9.86	− 9.10	− 1.14
M^*/M	0.70	0.64	0.60	0.52
U_0	62.2	79.0	94.2	122.2

TABLE 9

Binding energy of nuclear matter for the Bryan-Scott potential

	Potential energy per particle (MeV/A)				
k_F(fm^{-1}) State	1.35	1.52	1.58	1.62	1.74
$^1S_0$	−16.32	−20.31	−21.66	−22.53	−25.12
$^1D_2$	− 2.12	− 3.49	− 4.09	− 4.52	− 6.03
$^1G_4$	− 0.37	− 0.68	− 0.82	− 0.92	− 1.29
$^1I_6$	− 0.09	− 0.19	− 0.23	− 0.27	− 0.40
$^1P_1$	2.86	4.13	4.65	5.03	6.27
$^1F_3$	0.72	1.19	1.39	1.54	2.03
$^1H^5$	0.18	0.34	0.42	0.48	0.69
$^1J_7$	0.05	0.10	0.13	0.15	0.23
$^3S_1$	−16.90	−19.33	−19.99	−20.41	−21.49
$^3D_1$	1.40	2.32	2.72	3.02	4.04
$^3D_2$	− 3.59	− 5.83	− 6.80	− 7.51	− 9.90
$^3D_3$	0.15	0.25	0.30	0.34	0.46
$^3G_3$	0.18	0.35	0.43	0.49	0.70
$^3G_4$	− 0.62	− 1.16	− 1.41	− 1.60	− 2.27
$^3G_5$	0.07	0.14	0.18	0.21	0.31
$^3I_5$	0.03	0.07	0.09	0.10	0.16
$^3I_6$	− 0.14	− 0.29	− 0.37	− 0.42	− 0.64
$^3I_7$	0.01	0.03	0.04	0.05	0.08
$^3P_0$	− 3.56	− 4.79	− 5.21	− 5.48	− 6.24
$^3P_1$	9.39	14.72	17.08	18.82	24.75
$^3P_2$	− 7.84	−12.37	−14.27	−15.63	−20.19
$^3F_2$	− 0.50	− 0.90	− 1.08	− 1.21	− 1.68
$^3F_3$	1.35	2.33	2.77	3.09	4.22
$^3F_3$	− 0.30	− 0.62	− 0.79	− 0.92	− 1.40
$^3H_4$	− 0.07	− 0.15	− 0.19	− 0.22	− 0.34
$^3H_5$	0.28	0.56	0.70	0.80	1.17
$^3H_6$	− 0.03	− 0.08	− 0.10	− 0.12	− 0.18
$^3J_6$	− 0.01	− 0.03	− 0.04	− 0.05	− 0.08
$^3J_7$	0.07	0.15	0.19	0.23	0.36
$^3J_8$	− 0.01	− 0.02	− 0.02	− 0.03	− 0.04
totals					
S	−33.20	−39.64	−41.65	−42.93	−46.61
P	0.85	1.65	2.22	2.74	4.59
D	− 4.25	− 6.75	− 7.87	− 8.66	−11.43
F	1.27	2.00	2.29	2.51	3.17
G	− 0.74	− 1.15	− 1.62	− 1.83	− 2.56
H	0.36	0.67	0.83	0.95	1.34
I	− 0.18	− 0.38	− 0.46	− 0.54	− 0.80
J	0.09	0.20	0.26	0.29	0.47
$J \geqq 3$	1.45	2.29	2.68	2.93	4.06
$^3P_0+^3P_1+^3P_2$	− 2.01	− 2.48	− 2.43	− 2.29	− 1.68
P+D	− 3.40	− 5.10	− 5.65	− 5.92	− 6.84
total potential energy	−35.72	−43.32	−45.98	−47.50	−51.82
kinetic energy	22.68	28.56	31.07	32.66	37.68
total binding energy	−13.05	−14.77	−14.98	−14.84	−14.14
m^*	0.70	0.63	0.62	0.60	0.56
U_0	81.9	104.2	112.3	117.6	133.0

TABLE 10

Binding energy of nuclear matter for the Appel potential

	Potential energy per particle (MeV/A)				
k_F(fm^{-1}) State	1.20	1.50	1.68	1.80	2.10
$^1S_0$	−13.14	−20.18	−24.18	−26.61	−30.76
$^1D_2$	− 1.87	− 4.83	− 7.53	− 9.79	−16.64
$^3S_1$	−17.55	−23.21	−25.89	−27.54	−30.11
$^3D_1$	0.86	2.28	3.64	4.02	8.84
total binding energy	−13.78	−17.96	−18.83	−18.77	−13.80
M^*/M	0.58	0.52	0.50	0.49	0.45
U_0	76.8	120.1	145.3	161.5	207.4

TABLE 11

Binding energy (MeV/A) of nuclear matter for potentials A and B

	Force A				Force B			
k_F(fm^{-1}) State	1.36	1.50	1.80	2.10	1.36	1.50	1.80	2.10
$^1S_0$	−17.00	−20.58	−28.21	−34.85	−17.01	−20.58	−28.22	−34.88
$^1D_2$	− 1.09	− 1.92	− 5.21	−11.34	− 1.09	− 1.92	− 5.21	−11.35
$^1P_1$	2.92	4.62	9.98	17.09	2.91	4.62	9.96	17.07
$^3S_1$	−23.55	−28.89	−41.43	−54.08	−23.91	−28.79	−39.08	−48.23
$^3D_1$	1.81	2.72	5.73	10.79	2.28	3.40	6.66	11.01
$^3D_1$	− 4.21	− 6.27	−12.47	−21.25	− 3.29	− 5.10	−10.95	−19.72
$^3P_0$	− 3.15	− 4.12	− 6.12	− 7.57	− 3.15	− 4.12	− 6.12	− 7.58
$^3P_1$	11.20	15.94	29.27	46.80	11.20	15.93	29.26	46.78
$^3P_2$	− 8.84	−12.83	−24.44	−40.53	− 8.86	−12.85	−24.48	−40.59
$^3F_2$	− 0.17	− 0.29	− 0.62	− 0.70	− 0.17	− 0.29	− 0.62	− 0.71
$J \geqq 3$ [a]	1.92	2.94	6.26	10.91	1.92	2.94	6.26	10.91
totals								
S	−40.55	−49.47	−69.64	−88.93	−40.92	−49.37	−67.30	−83.12
P	2.11	3.60	8.79	15.80	2.10	3.57	8.72	15.68
D [b]	− 3.17	− 5.47	−10.76	−19.43	− 0.93	− 3.12	− 8.32	−17.69
F [c]	1.06	3.06	6.39	11.66	1.06	3.06	6.39	11.66
$^3P_0+^3P_1+^3P_2$	−0.81	− 1.02	− 1.19	− 1.29	− 0.81	− 1.05	− 1.25	− 1.39
P+D [b]	− 1.06	− 1.87	− 1.97	− 3.63	1.17	0.45	0.40	2.01
total potential energy	−40.17	−50.69	−67.26	−84.73	−39.19	−46.78	−62.56	−78.29
kinetic energy	23.03	28.01	40.34	54.90	23.03	28.01	40.33	54.90
total binding energy	−17.14	−20.68	−26.92	−29.82	−16.16	−18.76	−22.21	−22.38
M^*/M	0.60	0.55	0.48	0.44	0.57	0.52	0.49	0.46
U_0	105.0	130.4	194.0	265.0	103.0	128.3	183.3	242.0

[a] Taken from Reid values.
[b] Includes Reid $^3D_3$ contribution.
[c] Includes Reid $^1F_3$, $^3F_3$ and $^3F_4$ contributions.

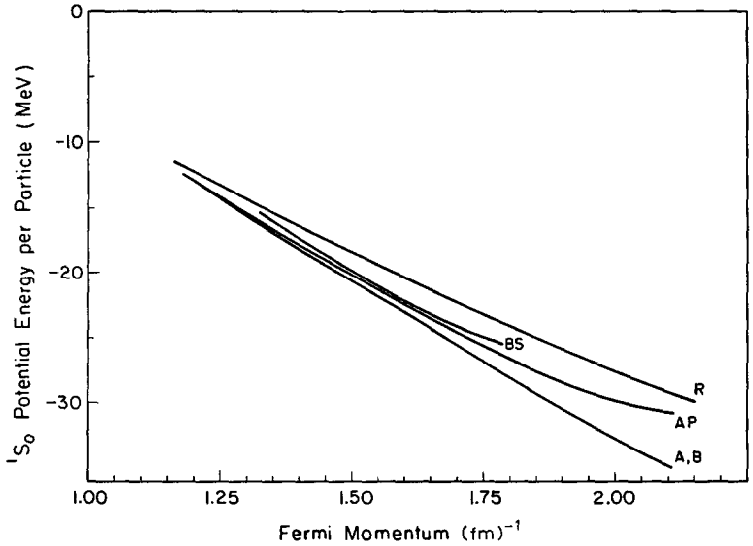

Fig. 14. The $^1S_0$ potential energy per nucleon as a function of density as measured by k_F, the Fermi momentum.

Drastic overbinding and collapse occurs only for the smoothest potentials (fig. 13 and table 7). It appears therefore that only strong potentials can produce proper nuclear saturation.

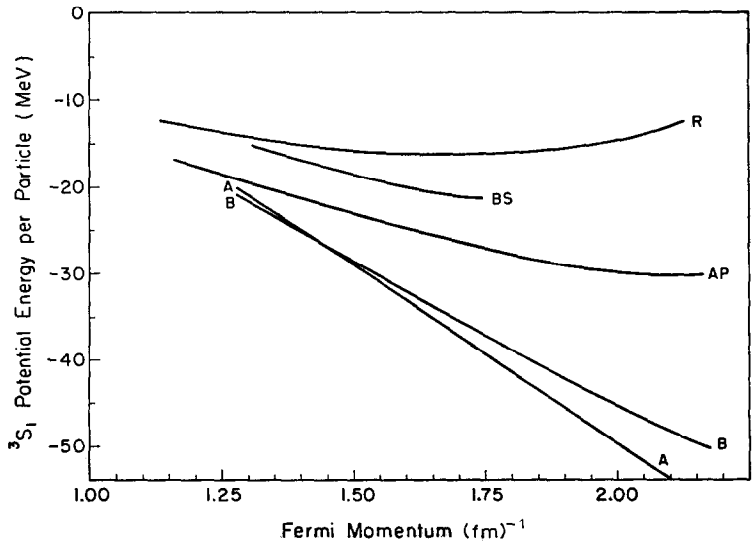

Fig. 15. The $^3S_1$ potential energy per nucleon as a function of density as measured by k_F, the Fermi momentum.

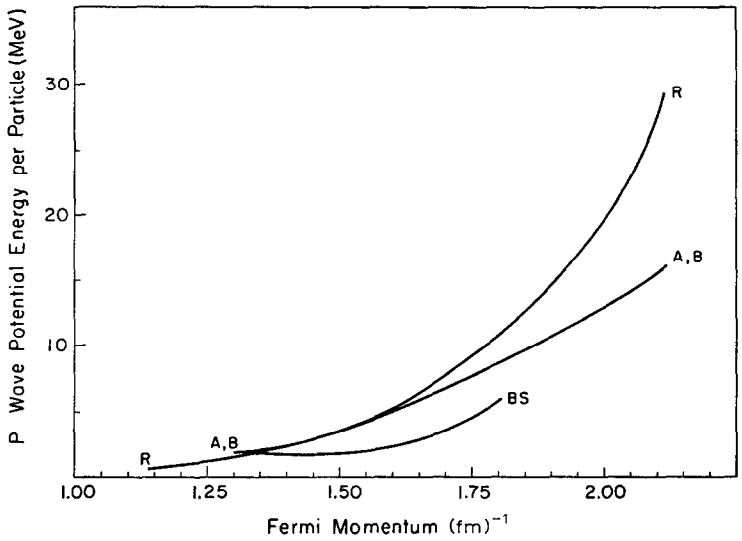

Fig. 16. The total P-wave potential energy per nucleon as a function of density as measured by k_F, the Fermi momentum.

The origin of the large overbinding for smooth potentials is shown in figs. 14–17 and tables 8–11. The pattern of more binding for smoother potentials is seen again for the $^1S_0$ and $^3S_1$ potential energies per particle. The net difference between the

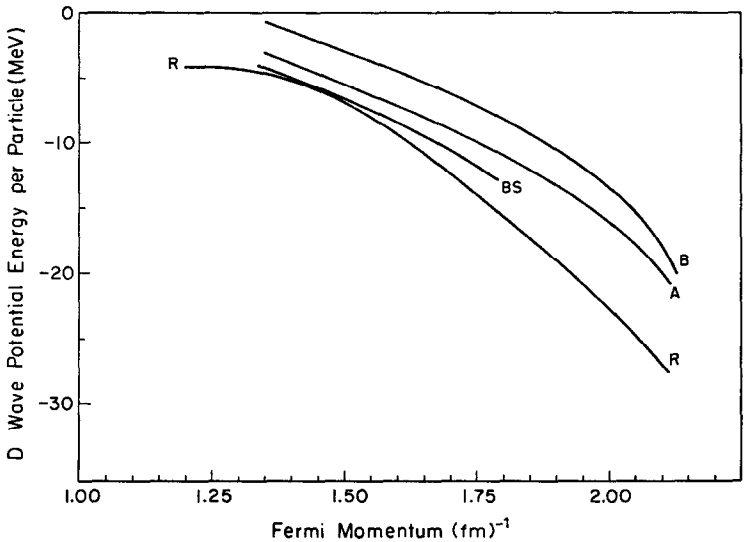

Fig. 17. The total D-wave potential energy per nucleon as a function of density as measured by k_F, the Fermi momentum.

Reid and potential A binding energies at $k_F = 1.8\,\mathrm{fm}^{-1}$ is enormous, about 25.3 MeV/A (fig. 15). At $k_F = 1.8\,\mathrm{fm}^{-1}$ the corresponding $^1S_0$ difference is 4.2 MeV/A; whereas the $^3S_1$ difference in binding is 25.6 MeV/A. (Figs. 14 and 15 and tables 8 and 11.)

The P- and D-wave contributions are shown in figs. 16 and 17. The net P-wave potential energy is repulsive, whereas the net D-wave terms are attractive. To some extent the different P- and D-wave values can be attributed to differences in the phase-shift fits. However, it is the S-waves that dominate the story.

The bulk of the overbinding obtained for smooth potentials comes from the $^3S_1$ contribution of an extra 25.6 MeV/A at $k_F = 1.8\,\mathrm{fm}^{-1}$. Furthermore, the potential energy from the sum of P-, D-, and F-waves (tables 8 and 11) gives about 4 MeV/A ($k_F = 1.8\,\mathrm{fm}^{-1}$) more repulsion for smoother potentials. This extra repulsion can compensate for the extra 4.2 MeV/A of attraction obtained for a smooth $^1S_0$ potential. It is therefore possible to eliminate the need for a strong $^1S_0$ repulsion, if higher (P+D+F) partial waves compensate for the gain in binding.

However, it is not possible to compensate for the extra binding of 25.6 MeV/A generated by a smooth $^3S_1+{}^3D_1$ potential. Thus smooth $^3S_1+{}^3D_1$ interactions produce overbinding and collapse and we conclude that strong $^3S_1+{}^3D_1$ potentials are required by saturation.

In particular, the tensor term of the $^3S_1+{}^3D_1$ potential must be strong. This requirement is seen by examining the changes in κ_{00}, κ_{02}, F_{00} and F_{02} [eqs. (5.5), (5.7)] that are generated by going from strong to weak potentials. When the $^1S_0$ potential undergoes a change of $\Delta\kappa_{00} = 0.0278$, the $^1S_0$ potential energy changes by 4.2 MeV/A at $k_F = 1.8\,\mathrm{fm}^{-1}$. This change is appreciably smaller than the corresponding $^3S_1+{}^3D_1$ increase of 25.6 MeV/A for $\Delta\kappa_{00} = 0.0363$ and $\Delta\kappa_{02} = 0.0704$ (table 7 and figs. 14, 15). These changes suggest that the main cause of overbinding is the use of weak tensor terms, rather than in the use of a smooth central term.

A further indication that the tensor force is playing the dominant role in saturation is seen in figs. 11 and 12. The $F_{02}(k)$ peak occurs at a lower value of $k(k^2 \approx 4\,\mathrm{fm}^{-2})$ than does the $F_{00}(k)$ peak ($k^2 \approx 9\,\mathrm{fm}^{-2}$). Therefore as the density increases and Q projects out states of increasing k, the tensor contributions enter first and are considerably altered by smooth nonlocalities. Alterations of $F_{00}(k)$ also change the saturation curve, but are less important at lower densities. It appears necessary for $F_{02}(k)$ to have a large peak at $k \approx 2\,\mathrm{fm}^{-1}$ to get a tensor-term saturation effect. Thus strong tensor terms are required by saturation.

The dominant tensor-term saturation effect shows up clearly for the Reid potential and to a lesser extent in the Bryan-Scott potential, i.e. the $^3S_1$ potential energy has a minimum (fig. 15). The saturation that results is $E/A = -9.9$ MeV/A, $k_F = 1.36\,\mathrm{fm}^{-1}$ for the Reid potential and $E/A = -15$ MeV/A with $k_F = 1.58\,\mathrm{fm}^{-1}$ for the Bryan-Scott potential. Both cases saturate because of their strong tensor terms and correspondingly their large values of κ_{02}. The saturation we obtain for the Reid case disagrees with the -11 MeV/A value obtained recently by Sprung *et al.* and by

Siemens [24]). Their use of the phase-shift approximation instead of the one-pion-exchange potential, for high partial waves accounts for the difference.

6. Conclusion

Matrix inversion in momentum space is a rapid and precise means of solving the Lippmann-Schwinger and Brueckner equations. It permits one to solve the two-body and nuclear matter problems for a large class of finite potentials, including nonlocal, local, weak, central and noncentral interactions.

A variety of potentials have been examined in this paper. They all produce approximately the same phase shifts, but have different wave functions. We have classified these potentials according to their smoothness, as measured by their wound integrals, $\kappa^{\alpha}_{LL'}$, and by the Bessel transforms of their wave function defects, $F^{\alpha}_{LL'}$. A systematic relationship between nuclear saturation and the smoothness of the two-nucleon potential is revealed.

It is found that smooth nonlocal potentials lead to overbinding and collapse. Furthermore, only strong potentials with strong tensor forces yield proper saturation. If one weakens the tensor interaction by introducing nonlocalities, a dramatic increase in binding and equilibrium density results.

Based on our calculations, we conclude that proper nuclear saturation can occur only if the $^3S_1+{}^3D_1$ wound integral satisfies the condition $0.05 \lessapprox \kappa_{02} \leqq 0.07$. Also, the quantity $F_{02}(k)$ must have a large peak to obtain saturation. That means the tensor force must be strong enough to easily excite nucleon pairs to $k \approx 2\ \mathrm{fm}^{-1}$. Higher order tensor terms appear therefore to be an inescapable requirement for proper nuclear saturation.

The use of smooth $^1S_0$ potentials also contributes to the overbinding and collapse of nuclear matter. Our calculations show that an increase of 4.2 MeV/A results from a change in $\kappa_{00}(^1S_0)$ of $\Delta\kappa_{00} = 0.0278$. This value is much less than the $^3S_1+{}^3D_1$ change of 25.6 MeV/A for $\Delta\kappa_{00} = 0.0363$ and $\Delta\kappa_{02} = 0.0704$. The $^1S_0$ increase of binding for smooth potentials can possibly be compensated by changes in the higher partial wave energies, but the large $^3S_1$ binding can only be reduced by using stronger tensor terms.

Recently, Coester *et al.* [25]) and Signell *et al.* [25]) have found similar changes in binding generated by changes in κ. Coester *et al.* [25]) deal with a set of exactly phase-shift equivalent potentials and are able to both increase and decrease the value of κ_{00} for a central interaction. They change $\kappa_{00}(^1S_0)$ by a large amount, $\Delta\kappa_{00} \approx 0.13$, and correspondingly induce a large $^1S_0$ change in binding of about 8 MeV/A. In preliminary calculations based on Coester's approach, we have found that the results presented here for approximately phase-shift equivalent potentials are reproduced using a set of potentials that give exactly the same phase shifts [16, 28]).

The fact that smoother potentials yield overbinding and collapse of nuclear matter has been suggested earlier by several authors [26]); the intimate connection between

saturation, $F^{\alpha}_{LL'}$, and κ has been pointed out before [7,10]; the need for a strong tensor force has also been previously stressed [12,24,27]. Our results confirm these conclusions and extend them to a larger class of potentials and larger changes in κ. The main surprise in these results is the extreme sensitivity to the tensor term.

An important feature of the methods described in this paper is that they can be used to examine the nonlocal, relativistic, and retardation aspects of one-boson-exchange potentials and their influence on nuclear binding [28].

We are grateful to Professors M. Baranger and R. M. Drisko for stimulating discussions. We thank Drs. D. Clement and F. Rybicki for their help with computer questions. The advice of Dr. R. V. Reid concerning Coulomb corrections to his phase shifts is greatly appreciated.

In performing the calculations reported in this paper, use was made of the University of Pittsburgh Computer Center, which is supported in part by the National Science Foundation under Grant No. G–9330.

Appendix

MOMENTUM SPACE MATRIX ELEMENTS OF THE REID-YUKAWA CORE AND BRYAN-SCOTT POTENTIALS

The momentum space matrix elements of the Reid and Bryan-Scott potentials involve the following three types of integrals:

$$I^{(1)}_{LL'}(k, k') \equiv \int_0^\infty r^2 \, \mathrm{d}r j_L(kr) \frac{\mathrm{e}^{-mr}}{r} j_{L'}(k'r), \tag{A.1}$$

$$I^{(2)}_{LL'}(k, k') = \int_0^\infty r^2 \, \mathrm{d}r j_L(kr) \left(\frac{m}{r} + \frac{1}{r^2}\right) \frac{\mathrm{e}^{-mr}}{r} j_{L'}(k'r), \tag{A.2}$$

$$I^{(3)}_{LL'}(k, k') = \int_0^\infty r^2 \, \mathrm{d}r j_L(kr) \left(m^2 + \frac{3m}{r} + \frac{3}{r^2}\right) \frac{\mathrm{e}^{-mr}}{r} j_{L'}(k'r). \tag{A.3}$$

For given L, L' k, k' only two of the $I^{(i)}_{LL'}(k, k')$ are linearly independent. The integral $I^{(1)}_{LL'}(k, k')$ is given by

$$I^{(1)}_{LL'}(k, k') = \frac{1}{2kk'} Q_L(z), \tag{A.4}$$

where $z = (k^2 + k'^2 + m^2)/2kk'$ and $Q_L(z)$ is a Legendre function of the second kind ($Q_L(z)$ satisfies the recursion relation $(L+1)Q_L + LQ_{L-1} = (2L+1)zQ_L$ and $Q_0(z) = \frac{1}{2} \ln ((z+1/z-1))$.

To evaluate $I^{(2)}_{LL'}(k, k')$, the relation

$$-\left(\frac{m}{r} + \frac{1}{r^2}\right) \frac{\mathrm{e}^{-mr}}{r} = \frac{1}{r} \frac{\mathrm{d}}{\mathrm{d}r} \frac{\mathrm{e}^{-mr}}{r} \tag{A.5}$$

is applied to (A.2); (A.2) is then integrated by parts. Various recursion relations of $j_L(kr)$, the spherical Bessel functions, are used and we obtain

$$I^{(2)}_{LL}(k, k') = \frac{-1}{2(2L+1)}(Q_{L+1}(z)-Q_{L-1}(z)). \tag{A.6}$$

Eq. (A.6) is the momentum space matrix element of the Thomas-type spin-orbit interaction.

Using

$$\left(m^2+\frac{3m}{r}+\frac{3}{r^2}\right)\frac{e^{-mr}}{r} = r\frac{d}{dr}\frac{1}{r}\frac{d}{dr}\frac{e^{-mr}}{r}, \tag{A.7}$$

along with integration by parts and recursion relation of $j_L(z)$, we find

$$I^{(3)}_{LL+2}(k, k') = \frac{k^2Q_{L+2}(z)+k'^2Q_L(z)}{2kk'} - Q_{L+1}(z).$$

To evaluate $I^{(1)}_{LL+2}(k, k')$ the result given by Davies [1])

$$I^{(1)}_{02}(k, k') = \frac{1}{4kk'^3}\left[6kk'+\tfrac{1}{2}(3m^2+k'^2-3k^2)\ln\left(\frac{z+1}{z-1}\right)\right.$$
$$\left.+6mk(\text{arc tg } m/(k+k')-\text{arc tg } m/(k-k'))\right] \tag{A.8}$$

is used, along with the recursion relations of $j_L(kr)$ to obtain the relation

$$\frac{k}{2L+3}(I^{(1)}_{LL+2}(k, k')+I^{(1)}_{L+2,L+2}(k, k') = \frac{k'}{2L+5}(I^{(1)}_{L+1,L+1}(k, k')+I^{(1)}_{L+1,L+2}(k, k')). \tag{A.9}$$

Using (A.4), we have

$$I^{(1)}_{L+1,L+3} = \frac{2L+5}{2L+3}\frac{k}{k'}\left(I^{(1)}_{LL+2}(k, k')+\frac{Q_{L+2}(z)}{2kk'}\right)-\frac{Q_{L+1}(z)}{2kk'}. \tag{A.10}$$

Since $I^{(1)}_{02}(k, k')$ is known from (A.8), we can determine $I^{(1)}_{13}(k, k')$, etc. Once $I^{(1)}_{LL}(k, k')$, $I^{(2)}_{LL}(k, k')$, $I^{(1)}_{LL+2}(k, k')$ and $I^{(3)}_{LL+2}(k, k')$ are known, we obtain $I^{(1)}_{LL}(k, k')$ and $I^{(2)}_{LL+2}(k, k')$ by linear combinations of the known integrals.

For large and small values of k, k' and z, the momentum space matrix elements must be computed with special care [ref. [16])] using expansions for $Q_L(z)/2kk'$.

References

1) T. Hamada and I. D. Johnston, Nucl. Phys. **34** (1962) 382;
R. V. Reid, Ph. D. Thesis, Cornell University (1968) and Ann. of Phys. **50** (1968) 411
2) F. Tabakin and K. T. R. Davis, Phys. Rev. **150** (1966) 793;
C. W. Nestor, K. T. R. Davies, S. J. Krieger and M. Baranger, Nucl. Phys. **A113** (1968) 14
3) P. Signell, The nuclear potential, in Advances in nuclear physics M. Baranger and E. Vogt, eds. Vol. 2, p. 223 (Plenum Press, New York, 1969)

4) H. P. Noyes, Phys. Rev. Lett. **15** (1965) 538;
K. Kowalski, Phys. Rev. Lett. **15** (1965) 798;
M. Scadron and S. Weinberg, Phys. Rev. **133B** (1964), 1589
5) R. A. Bryan and B. L. Scott, Phys. Rev. **177** (1969) 1435
6) K. Appel, Z. Phys. **219** (1969) 447
7) Some selected references on nuclear matter are: B. D. Day, Rev. Mod. Phys. **39** (1967);
M. Baranger, Proc. Int. School of Physics-Enrico Fermi (1967), course 40, p. 511;
G. Dahll, E. Ostgaard and B. Brandow, Nucl. Phys. **A124** (1969) 481
8) M. H. Kalos and R. H. Dalitz, Phys. Rev. **100** (1955) 1515;
P. Signell, Prog. Theor. Phys. (Kyoto) **49** (1959) 91;
M. Wada, Prog. Theor. Phys. (Kyoto) **41** (1969) 105 and **37** (1967) 763;
S. Machida, Supplement of Prog. of Theor. Phys. (Kyoto) **39** (1966) 91;
G. E. Brown, A. D. Jackson and T. T. S. Kuo, Nucl. Phys. **A133** (1969) 481
9) E. C. Bartels, A. K. Kerman and A. D. MacKellar, preprint (1969);
M. Reeves III and L. W. Owen, J. Computational Phys. **4** (1969) 572
10) K. A. Brueckner, C. A. Levinson and H. M. Mahmond, Phys. Rev. **95** (1954) 217
11) H. A. Bethe, B. H. Brandow, and A. G. Petshek, Phys. Rev. **129** (1963) 225;
R. Rajaraman and H. A. Bethe, Rev. Mod. Phys. **39** (1967) 745
12) D. W. Sprung, paper delivered at the Int. Conf. on atomic masses, University of Manitoba, Winnipeg, August 1967;
P. C. Bhargava and D. W. Sprung, Ann. of Phys. **42** (1967) 222;
A. Kallio and B. D. Day, Nucl. Phys. **A124** (1969) 177
13) M. Baranger, P. H. W. Kao, J. G. Depp (private communication);
M. Baranger Nuclear Structure with Realistic Interactions: A Survey of Methods and Recent Results (1969)
14) G. E. Brown and A. Green, Nucl. Phys. **A137** (1969) 1
15) E. J. Irwin, Ph. D. Thesis, Cornell University (1963)
16) M. I. Haftel, Ph. D. thesis, University of Pittsburgh (1969)
17) B. D. Day (private communication)
18) R. E. Peierls, Proc. Int. Conf. on nuclear structure, Kingston (University of Toronto Press, Toronto, 1960) p. 7;
M. Razavy, G. Field and J. S. Levinger, Phys. Rev. **125** (1962) 269;
A. M. Green, Nucl. Phys. **33** (1962) 218
19) F. Tabakin, Ann. of Phys. **30** (1964) 51
20) Reviews are given by: A. K. Kerman Nuclear Forces and Hartree-Fock Calculations, Summer School Course at Cargese (1968);
M. Baranger, Varenna Lectures [ref. 7)];
A. K. Kerman, J. P. Svenne and F. M. H. Villars, Phys. Rev. **147** (1966) 710;
D. M. Clement and E. Baranger, Nucl. Phys. **81** (1966) 241
21) A. K. Kerman, Proc. Int. Conf. on properties of nuclear states, Montreal (1969)
22) S. Okubo and R. E. Marshak, Ann. of Phys. **4** (1958) 166
23) R. E. Seamon, K. A. Friedman, G. Breit, R. D. Haracz, J. M. Holt and A. Prakash, Phys. Rev. **165** (1968) 1579
24) D. W. L. Sprung, P. K. Banerjee, A. M. Jopko and M. K. Srivastava, Nucl. Phys. **A144** (1970) 245;
P. J. Siemens, Nucl. Phys. **A141** (1970) 225
25) F. Coester, S. Cohen B. Day and C. M. Vincent, preprint (1969);
M. D. Miller, M. S. Sher, P. Signell and N. R. Yoder, Phys. Lett. **30B** (1969) 157;
also see E. Lomon Bull. Am. Phys. Soc. **14** (1969) 493
26) S. A. Moszkowski, Phys. Rev. **129** (1963) 1901;
M. A. Preston and R. K. Bhaduri, Phys. Lett. **6** (1963) 193;
C. W. Wong, Nucl. Phys. **56** (1964) 213; **71** (1965) 385
27) L. Ingber, Phys. Rev. **174** (1968) 1250
28) K. C. Richards, M. I. Haftel and F. Tabakin, Nucl. Phys. **A154** (1970) 1;
M. I. Haftel and F. Tababin; to be published